# Spectral properties of accreting millisecond pulsars obtained with the Comptonization model COMPPS

Master's thesis
University of Turku
Astronomy
2022
M.Sc. Julien Abou
Examiners:
Dr. Sergey Tsygankov
Prof. Juri Poutanen

The originality of this thesis has been checked in accordance with the University of Turku quality assurance system using the Turnitin OriginalityCheck service.

UNIVERSITY OF TURKU
Department of Physics and Astronomy

**Julien Abou** Spectral properties of accreting millisecond pulsars obtained with the Comptonization model COMPPS

Master's thesis, 53 pp.
Astronomy
March 2022

---

The neutron stars are unique objects to study properties of matter under extreme conditions. In fact, they are as dense as nuclear nuclei, at the same time they possess the highest magnetic fields in the Universe. Accreting millisecond pulsars are neutron stars in binary systems with optical companions. The companion feeds the compact object with matter, which accelerate the pulsar's rotational velocity. It finally reaches a period of a few milliseconds.

In this thesis, I performed a systematic spectral analysis of the full sample of accreting millisecond X-ray pulsars (AMXPs) observed in the broad energy range. Particularly, I reduced all available data obtained by the NuSTAR observatory. To widen the energy range, observations done by Swift/XRT or XMM-Newton observatories were added. The spectra are modelled with Comptonization model COMPPS. It allowed to fit successfully spectra of different AMXPs with only a few exceptions. For the sources where the model did not work correctly, it was possible to have a better result simply by adding a DISKBB component to the COMPPS one without the necessity to complicate the final model with more components. It was possible to show some correlation between spectral parameters and the source luminosity.

Moreover, as the COMPPS model has a gravitational redshift $z$ as a parameter, I compared the values obtained when it was fixed at 0 and when it was fixed at a more physically motivated value of 0.26. The redshift change increased the seed photon temperature $kT_{\rm bb}$ by approximately 30%. Also, the normalisation parameter decreased because the estimated radius source decreased with the redshift.

Keywords: neutron star, X-ray binary, pulsar, spectral analysis, Comptonization

# Contents

# 1 Introduction

The neutron stars (NSs) are one of the densest object in the Universe. By fitting the spectra obtained with observations of NSs, it is possible to access the physical properties of these objects. It is interesting for science because it gives access to an object as dense as atomic nucleus with a magnetic field which is impossible to reproduce in laboratory. The NSs are composed of a core surrounded by a thin crust composed of neutron rich nuclei.

The accreting millisecond X-ray pulsars (AMXPs) are a subclass of highly magnetised NSs which have a short rotational period in the order of milliseconds. They reside in old binary systems accreting matter from their companions leading to a growth of their rotational frequency after the initial slow down. It was in 1998 the X-ray transient SAX J1808.4–3658 was classified as the first AMXP by Rudy Wijnands and Michiel van der Klis [1]. This source was first observed in 1996 by the Rossi X-ray Timing Explorer. There is approximately 20 known AMXPs discovered during the past 2 decades. It is very few compared to the amount of radio pulsars already discovered by the different observatories.

In this thesis I will try to answer the question: Is it possible to fit all the AMXPs by using only one physical model? I will do it by taking a sample composed of AMXPs observations done by the NuSTAR observatory. In fact, NuSTAR allows to analyse the hard X-ray spectra between 3 and 78 keV. For the model, I will take the COMPPS comptonization model which is often used to fit the AMXPs spectra. Due to the strong gravity at the NS surface, the photons energy is gravitationally redshifted, the fact which is often ignored in the literature. The COMPPS model allows to fit a redshift value. I will also try to answer the question: Is it reasonable to let this parameter to be free or it is better to fix it at some specific value?

# 2 The millisecond pulsars

## 2.1 Neutron stars

A NS is the remnant collapsed core of a massive star ($M \gtrsim 8\ M_\odot$). At the end of its life, the center of a massive star has fused all elements lighter than iron, then there is an iron core held up by electron degeneracy pressure. When the core mass excess the Chandrasekhar mass ($\sim 1.4\ M_\odot$), it starts to collapse because the pressure is not anymore sufficient to assure the hydro-static equilibrium. During the collapse, the core radius decreases, so its density $\rho$ increases. When the collapse begins, $\rho \sim 10^6$ g cm$^{-3}$. The neutronization begins at $\rho \sim 10^7$ g cm$^{-3}$. Then, the nuclei in the core become neutron rich and because the density continues to increase, the neutrons start to become free. At $\rho \sim 10^{10}$ g cm$^{-3}$, the neutron degeneracy pressure becomes important. It is this pressure which halt the collapse when $\rho \sim 10^{14}$ g cm$^{-3}$. At this stage, the mass is about 1.4 $M_\odot$ for a radius of 10 km. A NS is composed of an inner core, where the density exceeds the standard nuclear one. Its exact composition is unknown. The outer core is composed of neutrons and protons in Fermi liquid. Electrons, neutrons and nuclei can be found in the crust.

The NSs have one of the highest magnetic field in the Universe. In fact, the initial stellar magnetic field is amplifying during its collapse and finally reaches a value about $10^{12}$ G. As the angular momentum $L = I\,\omega$ is conserved and the moment of inertia $I$ is proportional to $MR^2$, the NSs have a very high spin angular frequency due to their compactness. The high rotation speed and magnetic field strength allow an intense Lorentz force which will extract positrons and electrons from the NSs surface. Due to the particles extractions, a synchrotron emission is emitted from the NSs. It is visible in the radio band. The rotational energy of the

NSs will decrease with time due to the magnetic dipole radiation:

$$P_{\rm rad} = \frac{2}{3c^3} \left(BR^3 \sin\alpha\right)^2 \left(\frac{2\pi}{P}\right)^4, \tag{1}$$

where $c$ is the speed of light, $B$ the magnetic field strength, $R$ the NS radius and $P$ its spin period. The rotational energy loss is:

$$\dot{E} = -\frac{4\pi^2 I \dot{P}}{P^3}. \tag{2}$$

We can then relate the magnetic field strength $B$ with the spin period $P$ and its time derivative:

$$B \propto \sqrt{P\dot{P}}. \tag{3}$$

So, it is possible to follow the evolution of a NS by using a $P-\dot{P}$ diagram (Figure 1). A NS borns in the left part with a fast spin period and strong magnetic field. Then, the spin period increases with time. The NS evolves to the right of the diagram. When the NS rotates too slowly to assure enough power for the emission, it enters the so-called "graveyard" (Bottom right in the $P-\dot{P}$ diagram, Figure 1) where it is not visible any more.

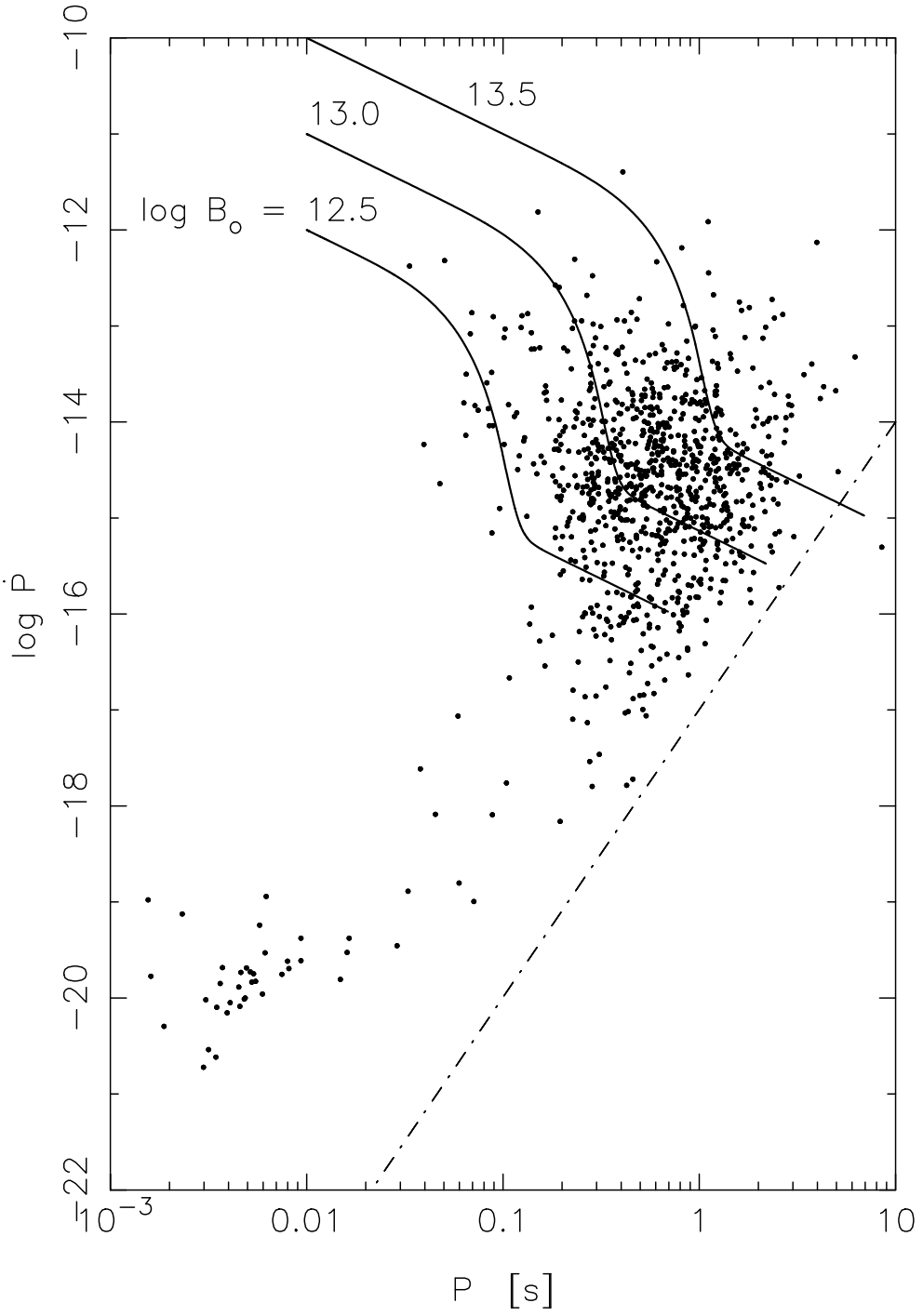


Figure 1: Evolution of pulsars in the $P - \dot{P}$ diagram for different initial magnetic fields. The dotted line delimits the graveyard in the bottom right [2].

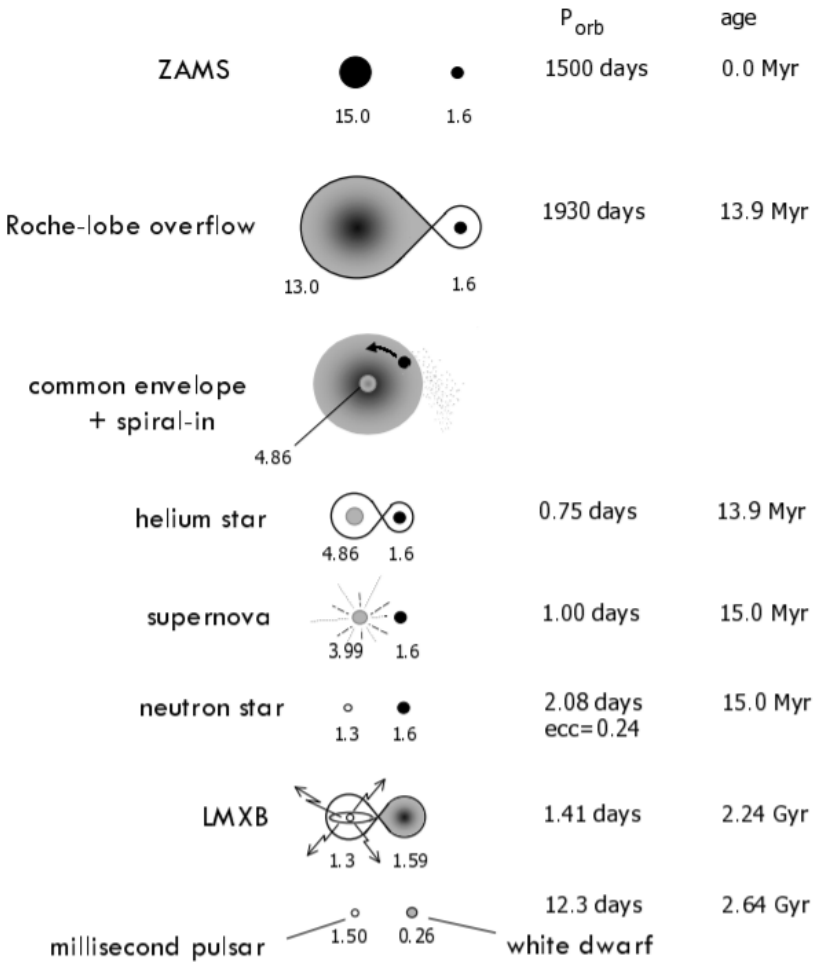


Figure 2: Evolution of a typical binary system where the stars are created together. Masses are given in solar masses. ZAMS = Zero Age Main Sequence [3].

## 2.2 X-ray binary systems

The X-ray binaries are systems where a compact object such as a NS or a black hole accretes matter from another star. The stars in an X-ray binary system are generally born together. Then, they evolve together until one of them (the most massive) becomes a NS after a supernova explosion (Figure 2).

In a dense stellar region like clusters, an isolated NS can also capture another star to form a binary system by tidal capture. Let's consider a compact star of mass $m$, a target star of mass $M$ and radius $R$. Their relative velocity is $v$. The relative

kinetic energy of the system is:

$$E_k = \frac{1}{2}\,\frac{Mm}{M+m}\,v^2. \tag{4}$$

When approaching the target star, a tidal bulge will be formed on the compact star. Its mass is $m_t$ and its height is $h$. The potential energy of the bulge is:

$$E_t \sim m_t\,\frac{GM}{R^2}\,h. \tag{5}$$

The target star will capture the compact one if $E_t > E_k$.

The X-ray binary systems are divided mainly into two different categories: High mass (HMXB) and Low mass (LMXB). The High mass binaries have a high mass companion, like an O or B star. In contrary, the low mass binaries have small stars as companions, and as a rule such systems are much older. Concerning the orbital period, it is longer in HMXBs. In fact, as the companion star is bigger in a HMXB, its distance from the NS is higher.

The matter between the two objects can be accreted in two ways (Figure 3): by Roche lobe overflow if the companion star is bigger than its Roche lobe (LMXBs). In that case, the matter fall into the compact one via the inner Lagrangian point. Due to the rotation of the system, the matter has a great angular momentum and starts to rotate around the NS creating an accretion disk. Another way to accrete matter is via wind. It happens if the companion star does not exceed its Roche lobe (HMXBs). In that case, a part of the matter lost by the companion is gravitationaly captured by the compact star.

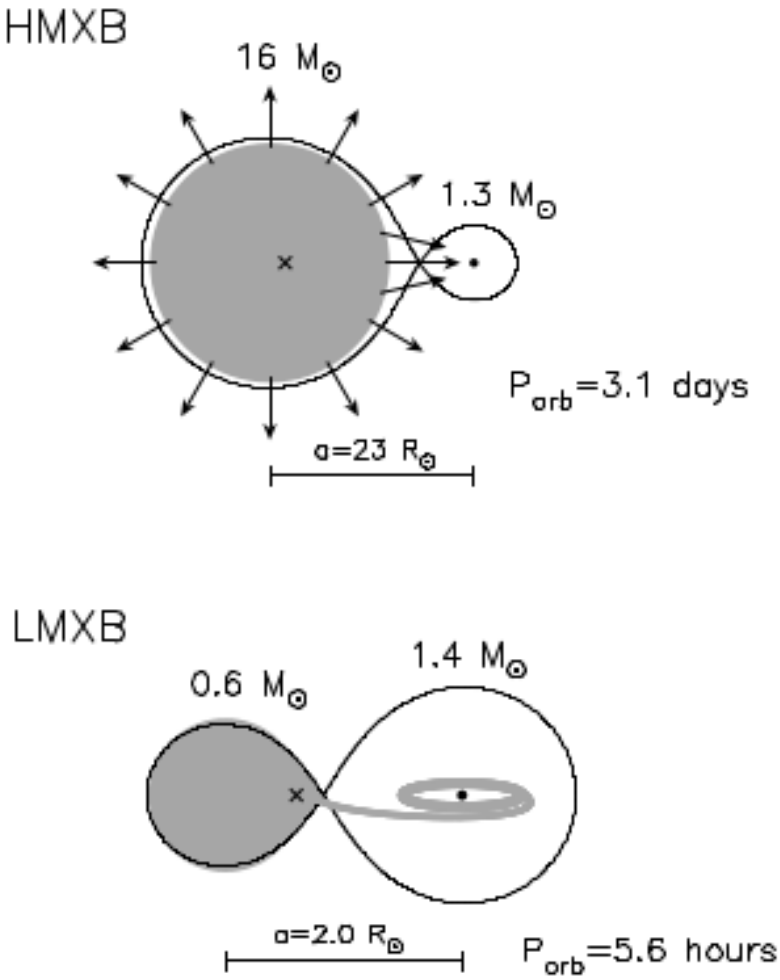


Figure 3: Typical HMXBs and LMXBs. In HMXB, the NS is fed by wind accretion and in LMXB it is mainly fed by Roche-lobe overflow [3].

## 2.3 Millisecond pulsars

The accreting millisecond pulsars are NSs in a binary system. So, after the NS has lost rotational power for emitting radiation and is in the graveyard, it can be fed by the accreted matter from its companion via Roche lobe overflow. Its spin period will decrease due to the angular momentum of the matter. The co-rotation radius of the NS is:

$$R_C = \left( \frac{G\,M\,P^2}{4\,\pi^2} \right)^{1/3}, \tag{6}$$

where $G$ is the gravitational constant, $M$ the NS mass and $P$ its spin period. The matter will accreate if this radius is greater than the Alfvén radius corresponding to the equilibrum between the ram pressure of the matter and the magnetic pressure:

$$R_A = \left( \frac{B^4\,R^{12}}{8\,G\,M\,\dot{M}^2} \right)^{1/7}, \tag{7}$$

where $B$ is the magnetic field strength, $R$ - the NS radius and $\dot{M}$ - the accretion rate. A stable spin period is obtained when the both radii are the same: $R_A = R_C$. This period depends then on the magnetic field strength and the accretion rate as follow:

$$P \propto B^{6/7}\,\dot{M}^{-3/7}. \tag{8}$$

With the acceleration of its rotation, the pulsar evolves from the graveyard to the left of the $P - \dot{P}$ diagramm and becomes visible again as an accreting millisecond pulsar on the bottom left of Figure 1.

The energy produced by the accretion of a mass $m$ on a body surface of mass $M$ and radius $R$ is:

$$E_{accretion} \sim \frac{G\,M\,m}{R}. \tag{9}$$

For the mass and radius of a typical NS ($R \sim 10$ km and $M \sim 1.4$ $M_\odot$), it gives:

$$E_{accretion} \sim 1.9 \cdot 10^{20} \text{ erg g}^{-1}.$$

After accreted about 0.1 $M_\odot$, the period will be a few milliseconds [4]. This model is called the recycling scenario.

The millisecond pulsars (MSP) have a weak magnetic field and their spin period is rapid compared to most of the pulsars. They can be separated in different systems depending of the target star's mass and the orbital period ($P_b$):

- Ultra compact system with $P_b \lesssim 80$ minutes, the companion star is a white dwarf.
- Compact system when 1.5 h $\lesssim P_b \lesssim$ 3 h, the companions are brown dwarfs.
- Wider systems with 3.5 h $\lesssim P_b \lesssim$ 20 h and main sequence stars companions.

## 2.4 Emission mechanism in AMXPs

When the NS rotates around its companion star, it accretes some matter. Due to the extreme gravity of the NS, the matter (hydrogen) is accreted by Roche lobe overflow and create an accretion disk around the compact star. The hydrogen can also reach the surface then it is converted into helium which will be accumulated in a layer around the NS. When there is enough Helium around the star, an explosion heats the surface and an X-ray burst (Type I) is produced. Bursts are generally separate by time intervals from hours to days. Between those outbursts, the pulsar is in quiescence and its luminosity decreases.

During the accretion phase, when the matter gets closer to the NS, a part of its mechanical energy is dissipated and emits a black-body spectrum. Generally, AMXPs present in their X-ray spectra one or two black body components and a comptonization one. Most of the time, this latest has cutoff energies which are linked to the electron temperature of the corona. In this situation, it is expected the hard comptonization photons from the cold accretion disk are reflected. Then, the reflection results in appearance of Iron lines in the spectra around 6-7 keV. The hard photons will also create a continuum spectrum if they hit the disk because they will be scattered by Thompson or Compton effect. It is the Compton hub and it could be seen in spectrum as an emission excess from 10 to 30 keV.

## 2.5 The COMPPS spectral model

The COMPPS spectral model was used to model the observations of the sample of AMXPs. It was developed by Juri Poutanen and Roland Svensson in 1996 [5]. The model has 19 parameters which are reported in table I. The goal is to solve the comptonization and the radiative transfer in a disk corona model for X-ray binaries (and also for the active galactic nuclei). A two phase disk-corona model is considered with a hot corona above an optically thick plane-parallel cold disk. The model can describe the hot corona as a plane-parallel slab, an hemisphere or a cylinder. The energy dissipation can both occur in the hot corona and in the cold disk. Following that, the radiation from the cold disk combines a radiation from the hot corona and a radiation due to energy dissipation in the cold disk ($T_{disk}$). The corona can include a background plasma or be a pure pair one. The electrons and positrons are assumed to have a Maxwellian distribution.

This model allows to fix a gravitational redshift. As it is generally the case in literature, I fixed it at 0 (default parameter) for each observation in my first model. Nevertheless, due to the strong NSs gravitational field, the emitted photons are shifted by the gravitational redshift. In a second model, I fixed the redshift at a realistic value to be able to compare the new parameters values to the first ones. To calculate the redshift value, I considered the classical parameters for a NS: $M \sim 1.5$ $M_\odot$ and $R \sim 12$ km.

Table I: Parameters for the COMPPS model

| Parameter name | Parameter symbol | Unit | Initial value | State of the parameter |
|---|---|---|---|---|
| Electron temperature | $kT_{\rm e}$ | keV | 40 | Free |
| Electron power-law index | Ele Index | | 2 | Frozen |
| Minimum Lorentz factor | $\rm G_{min}$ | | -1 | Frozen |
| Maximum Lorentz factor | $\rm G_{max}$ | | 1000 | Frozen |
| Temperature of soft photons | $kT_{\rm bb}$ | keV | 1 | Free |
| Vertical optical depth of the corona | $\tau$ | | 2 | Free |
| Geometry (1) | geom | | 1 (2) | Frozen |
| Cosine of inclination angle | cos Incl | | 0.5 | Frozen |
| Covering factor of cold clouds | cov frac | | 1 | Frozen |
| Amount of reflection | rel refl | | 0 | Frozen |
| Iron abundance | Fe ab | Solar | 1 | Frozen |
| Abundance of heavy elements | Me ab | Solar | 1 | Frozen |
| Disk ionization parameter | $\xi$ | | 0 | Frozen |
| Disk temperature for reflection | $T_{\rm disk}$ | K | $10^6$ | Frozen |
| Reflection emissivity law | Betor10 | | -10 (3) | Frozen |
| Inner radius of the disk | $\rm R_{in}$ | Schwarzschild | 10 | Frozen |
| Outer radius of the disk | $\rm R_{out}$ | Schwarzschild | 1000 | Frozen |
| Gravitational redshift | Redshift | | 0 | Frozen |

(1) Geometry to estimate the escape probability for the radiative transfer calculation (2) Slab geometry (3) Non-rotating disk

The gravitational redshift $z$ is given by:

$$1 + z = \frac{1}{\sqrt{1 - \dfrac{2\,GM}{Rc^2}}}, \tag{10}$$

where $G$ is the gravitational constant, $M$ - the mass of the NS, $R$ - its radius and $c$ - the light velocity:

$$z \sim 0.26$$

In the second model, all the data and fixed parameters are the same as in the first one, with the exception of the gravitational redshift changed from 0 to 0.26.

# 3 Observations and sample of sources

## 3.1 Observatories and data reduction

### 3.1.1 NuSTAR X-ray observatory

The Nuclear Spectroscopic Telescope Array (NuSTAR) is a space X-ray observatory launched on the $13^{th}$ June 2012. It is the first one focusing hard X-rays from 3 to 79 keV. Two optics modules are on-board (OMA and OMB), composed of 133 mirror shells. Each optical module is focusing emission to a corresponding focal plane module (FPMA and FPMB, respectively). The field of view covers a square of 12.2' length with an angular resolution of 18". The spectral resolution varies from 400 eV at 10 keV to 900 eV at 68 keV. The event timing is about few milliseconds and the maximum readout of them is 400 $s^{-1}$.

I used Nupipeline in Heasoft to reduce the data. The software version was heasoft-6.28 with Nupipeline 0.4.8, nustardas 2.0.0 and calibration data CALDB20210202. The spectra have been obtained with Nuproducts.

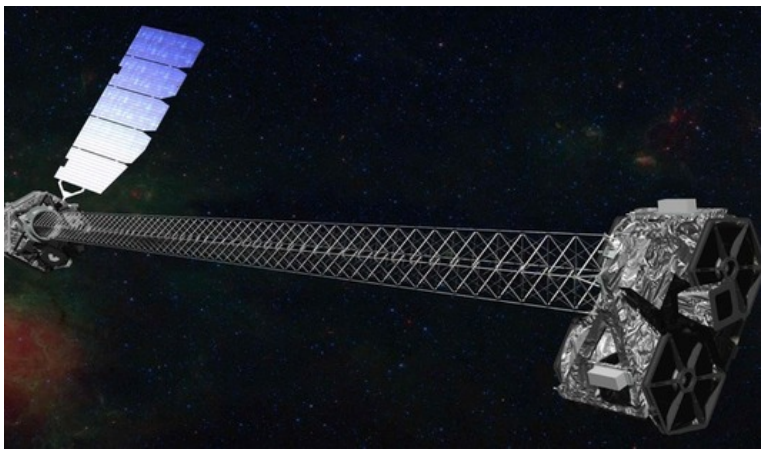

Figure 4: The NuSTAR observatory

### 3.1.2 XMM-Newton observatory

The XMM-Newton space observatory was launched by the European Space Agency on $10^{th}$ December 1999. Its orbit is very elliptical and the distance to Earth varies from 7000 km at the perigee to 114 000 km at the apogee. It allows to work outside the Van Allen radiation belts. 3 instruments are on-board of XMM-Newton:

- The European Photon Imaging Camera (EPIC) for X-ray imaging covering the 0.2-12 keV range with a Field Of View of 30'. Two types of CCD cameras composed the EPIC instrument: Two Metal Oxide Semiconductor (MOS) and a PN camera. Each MOS camera is composed of 7 CCDs and the PN camera - of 12 CCDs.

- The Optical Monitor (OM): It is a co-aligned 30 cm UV / Optical telescope composed of 3 UV and 3 Optical filters covering the 180-600 nm range. This telescope is used to obtain simultaneous multi-wavelengths observations with XMM-Newton observatory.

- The Reflection Grating Spectrometers (RGS) for X-ray spectroscopy covering the 0.33-2.5 keV range.

For the XMM-Newton observations, I obtained the MOS spectra with the interactive analysis tool on the XMM-Newton science archive website. As the PN spectra are not available for the online analysis, I used the Science Analysis Software (SAS) to reduce these observations. The SAS release used was the version 19.1.0 and I downloaded the calibration files on the website on the $11^{th}$ May 2021.

### 3.1.3 The Neil Gehrels Swift Observatory

Swift was launched on $20^{th}$ November 2004. The main purpose of the mission is to observe a large number of Gamma-Ray Bursts (GRB): Determine their origin, classify them and discover new types. Also, the hard X-ray survey of the sky has been performed by Swift.

3 instruments of the Swift observatory:

- The Burst Alert Telescope (BAT). It covers a hard X-ray band (15 - 150 keV) and it allows to detect the GRBs.
- The X-ray Telescope (XRT) is aimed at studying the X-ray emission following the detections by BAT. It covers the energy range from 0.2 to 10 keV.
- The Ultraviolet and Optical Telescope (UVOT) covering wavelengths from 170 to 650 nm.

I used the XRT data to broaden the NuSTAR energy range below 3 keV. The online tools were used to get the spectra from Swift/XRT observations. When it was impossible to get the spectrum online, I reduced the observations by using the XRT pipeline version 0.13.5 and XSelect version 2.4k in HEASoft.

## 3.2 Data

The sample is composed of all AMXPs already observed with the NuSTAR observatory. It represents 13 sources from about 20 currently known AMXPs. The observations available for NuSTAR are reported in table II. A source can have multiple observations. Some of them are not in the sample if, after reduction, the spectra obtained did not allow to get an acceptable approximation due to low statistics. The transitional millisecond pulsars which were not in accretion-powered phase were excluded: It includes PSR J1023+0038 in June 2013 [6] and XSS J12270−4859 [7]. To get the soft energy spectra below 3 keV, I used the Swift/XRT or the XMM-Newton observations. The available observations performed in a reasonable time compared to the NuSTAR ones (some days before or after) are also reported in table II. All the spectra were binned to achieve a minimum of 25 photons per bin.

Table II: Observations of AMXPs

| Source Name | NuSTAR obs ID | NuSTAR obs date (yy-mm-dd) | NuSTAR Exposure time (s) | XMM-Newton obs ID | XMM-Newton obs date (yy-mm-dd) | XMM-Newton Exposure time (s) | Swift obs ID | Swift obs date (yy-mm-dd) | Swift/XRT Exposure time (s) |
|---|---|---|---|---|---|---|---|---|---|
| Swift J1756.9−2508 | 90402313002 | 18-04-08 08:31:09 | 39476 | 0830190401 | 18-04-08 01:49:54 | 65966 | 00088662001 | 18-04-08 18:23:57 | 2201 |
| Swift J1756.9−2508 (1) | 90402313004 | 18-04-14 02:56:09 | 60978 | 0830190401 | 18-04-08 01:49:54 | 65966 | 00088662002 | 18-04-14 19:29:57 | 2118 |
| Swift J1756.9−2508 | 90501329001 | 19-06-22 07:51:09 | 37738 | | | | 00030952025 | 19-06-21 00:35:36 | 910 |
| IGR J17591−2342 | 90401331002 | 18-08-13 22:36:09 | 27085 | 0795750101 | 18-09-03 17:49:09 | 36700 | 00010804002 | 18-08-14 00:35:56 | 660 |
| IGR J17591−2342 | 80301311002 | 18-08-17 20:01:09 | 29168 | 0795750101 | 18-09-03 17:49:09 | 36700 | 00010804004 | 18-08-18 05:13:58 | 466 |
| IGR J00291+5934 | 90101010002 | 15-07-28 12:46:08 | 38103 | 0744840201 | 15-07-28 11:48:19 | 86563 | 00031258006 | 15-07-29 00:18:11 | 1429 |
| IGR J1737.9−3747 | 90401312002 | 18-04-02 02:41:09 | 37360 | 0830190301 | 18-04-01 01:18:01 | 48100 | 00031270007 | 18-04-02 14:19:57 | 1132 |
| IGR J1737.9−3747 (1) | 90601333002 | 20-10-18 11:51:09 | 19877 | | | | 00031270044 | 20-10-18 00:48:35 | 1532 |
| IGR J16597−3704 | 90301324001 | 17-10-26 12:16:09 | 42214 | | | | 00010364002 | 17-10-25 07:28:57 | 979 |
| IGR J17062−6143 | 30101034002 | 15-05-06 19:26:07 | 70110 | | | | 00037808005 | 15-05-06 23:24:58 | 920 |
| IGR J17062−6143 | 30201018002 | 16-09-13 08:46:08 | 66600 | 0790780101 | 16-09-13 12:03:52 | 64900 | 00081872001 | 16-09-13 10:56:57 | 1964 |
| IGR J17511−3057 | 90101001002 | 15-04-08 20:36:07 | 42241 | 0770580301 | 15-03-26 21:59:27 | 78200 | 00031492033 | 15-04-08 10:07:58 | 1459 |
| MAXI J0911−655 | 90201024002 | 16-05-24 00:31:08 | 59897 | 0790181501 | 16-05-22 13:23:12 | 37800 | 00081952001 | 16-05-24 12:49:58 | 1754 |
| MAXI J0911−655 | 90201042002 | 16-11-23 15:26:08 | 33757 | | | | 00088013001 | 16-11-23 20:57:58 | 1981 |

Table II: Observations of AMXPs (Continued)

| Source Name | NuSTAR obs ID | NuSTAR obs date (yy-mm-dd) | NuSTAR Exposure time (s) | XMM-Newton obs ID | XMM-Newton obs date (yy-mm-dd) | XMM-Newton Exposure time (s) | Swift obs ID | Swift obs date (yy-mm-dd) | Swift/XRT Exposure time (s) |
|---|---|---|---|---|---|---|---|---|---|
| PSR J1023+0038 (2) | 30001027002 | 13-06-10 13:16:07 | 13393 | | | | 00080035001 | 13-06-10 13:59:59 | 1955 |
| PSR J1023+0038 (2) | 30001027003 | 13-06-10 21:16:07 | 33754 | | | | 00080035001 | 13-06-10 13:59:59 | 1955 |
| PSR J1023+0038 (2) | 30001027005 | 13-06-12 05:36:07 | 47964 | | | | 00080035002 | 13-06-12 21:59:59 | 1899 |
| PSR J1023+0038 | 30001027006 | 13-10-19 07:56:07 | 94268 | 0720030101 | 13-11-10 15:42:34 | 138100 | 00080035003 | 13-10-18 05:07:59 | 9966 |
| PSR J1023+0038 | 30201005002 | 16-05-07 15:21:08 | 87288 | 0784700201 | 16-05-08 03:29:38 | 127900 | 00092401001 | 16-05-08 18:41:58 | 9633 |
| PSR J1023+0038 | 80201028002 | 17-05-23 00:21:09 | 82514 | 0794580801 | 17-05-23 21:24:11 | 26000 | 00033012149 | 17-05-23 21:53:57 | 1740 |
| PSR J1023+0038 | 90301006002 | 17-06-13 12:06:09 | 26820 | 0803620501 | 17-06-13 13:39:02 | 24000 | 00033012166 | 17-06-13 04:12:12 | 2043 |
| SAX J1748.9−2021 | 90001002002 | 15-02-26 17:46:07 | 18172 | 0748391301 | 15-03-04 12:56:48 | 117400 | 00081435001 | 15-02-26 21:31:59 | 1923 |
| SAX J1748.9−2021 | 90301320002 | 17-10-11 21:11:09 | 44470 | 0795712201 | 17-10-09 10:14:49 | 61300 | 00010341005 | 17-10-11 18:59:59 | 983 |
| SAX J1808.4−3658 | 90102003002 | 15-04-15 01:01:07 | 49264 | 0724490201 | 15-04-11 03:01:49 | 109000 | 00030034077 | 15-04-15 17:46:01 | 839 |
| SAX J1808.4−3658 | 90102003004 | 15-05-09 23:16:07 | 21507 | 0724490201 | 15-04-11 03:01:49 | 109000 | 00030034088 | 15-05-09 23:19:59 | 975 |
| SAX J1808.4−3658 (1) | 90102003006 | 15-06-13 18:31:07 | 83812 | | | | 00033801010 | 15-06-14 00:40:58 | 2139 |
| SAX J1808.4−3658 | 90501335002 | 19-08-10 11:11:09 | 41025 | 0804330201 | 19-09-07 01:46:33 | 35300 | 00033801025 | 19-08-09 16:30:35 | 964 |
| Swift J1749.4−2807 | 90701310002 | 21-03-04 07:11:09 | 49394 | 0872392001 | 21-03-04 00:14:50 | 57800 | | | |
| XSS J12270−4859 (2) | 30101033002 | 15-04-26 01:06:07 | 89979 | | | | 00081457001 | 15-04-25 17:03:58 | 1969 |

(1) Observation not in sample due to low available statistics. (2) Transitional pulsar not in accretion-powered mode, not in sample.

## 3.3 Description of the selected sources

### 3.3.1 Swift J1756.9−2508

Swift J1756.9−2508 is a low mass X-ray binary pulsar discovered in June 2007 with the BAT instrument of the Swift observatory. The companion star is an helium dominated white dwarf with a mass estimated to be between 0.0067 and 0.03 $M_\odot$ [8]. In 2018, Sanna et al. estimated the magnetic field of the NS between 3.1 and $4.6 \cdot 10^8$ G [9].

### 3.3.2 IGR J17591−2342

IGR J17591−2342 was discovered during its outburst in June 2018 by INTEGRAL. Assuming the NS mass is 1.4 $M_\odot$, the magnetic field is in the range $1.4 \cdot 10^8$ - $8 \cdot 10^9$ G. The companion star is an old 8-12 Gyr main sequence star with mass estimated to be between 0.85 and 0.92 $M_\odot$ [10].

### 3.3.3 IGR J00291+5934

IGR J00291+5934 was detected during an outburst in December 2004 by INTEGRAL. Assuming a 1.4 $M_\odot$ NS, the companion star is probably a low mass (0.04 $M_\odot < M_* < 0.16\ M_\odot$) brown dwarf star. Torres et al. found a magnetic field strength smaller than $3 \cdot 10^8$ G [11].

### 3.3.4 IGR J1737.9−3747

IGR J1737.9−3747 is an X-ray transient in a low mass binary system discovered by INTEGRAL on $17^{th}$ February 2004. It was only catalogued as an AMXP in 2018 [12]. The minimum companion mass is 0.055 $M_\odot$ with a 1.4 $M_\odot$ NS. This source has unusual strong pulsations and soft phases lags [13].

### 3.3.5 IGR J17511−3057

IGR J17511−3057 was discovered in 2009 by INTEGRAL. It is an AMXP in a binary system with a 3.47 h orbital period. The companion star has a mass between 0.15 and 0.44 $M_\odot$. The magnetic field is weaker than $3.5 \cdot 10^8$ G [14].

### 3.3.6 MAXI J0911−655

MAXI J0911−655 was detected in the globular cluster NGC 2808 on $19^{th}$ February 2016 by the MAXI/GSC system. Few days later, the position was confirmed by the Burst Alert Telescope on boarded on Swift observatory. By assuming a NS of 1.4 $M_\odot$, the companion mass has been estimated greater than 0.024 $M_\odot$. In 2017, Sanna et al. found it was compatible with a brown dwarf older than $5 \cdot 10^9$ years [15].

### 3.3.7 PSR J1023+0038

PSR J1023+0038 was first detected by the FIRST survey (Faint Images of the Radio Sky at Twenty Centimeters) in 2002. At this moment, it was classified as a magnetic cataclysmic variable [16]. In 2009, following the survey of the Green Bank Telescope proceeded 2 years before, it was finally classified as a millisecond pulsar [17]. PSR J1023+0038 is in a binary system with a 0.2 $M_\odot$ companion. The pulsar had an accretion disk in early 2000's [17]. It is a transitional pulsar swinging between radio and X-ray phases.

### 3.3.8 SAX J1748.9−2021

SAX J1748.9−2021 was detected by BeppoSAX observatory during an X-ray activity monitoring in the galactic centre in 1998. The companion star should be a main sequence star with a mass between 0.85 and 1.1 $M_\odot$ [18].

### 3.3.9 SAX J1808.4−3658

SAX J1808.4−3658 was observed for the first time by BeppoSAX in 1996. Its nature was unknown during 2 years until pulsations in the millisecond range were discovered in 1998 [1]. Following that, SAX J1808.4−3658 became the first known AMXP. In 2001, Bildsten and Chakrabarty found the companion star was a brown dwarf with mass of 0.05 $M_\odot$ [19].

### 3.3.10 Swift J1749.4−2807

Swift J1749.4−2807 was detected during an X-ray burst in 2006 by the Swift/BAT instrument. It was classified as an accreting millisecond pulsar after an Rossi X-ray Timing Explorer observation on $14^{th}$ April 2010 [20]. The companion has a minimum mass of 0.475 $M_\odot$ with a NS of 1.4 $M_\odot$ [21].

### 3.3.11 IGR J16597−3704

IGR J16597−3704 is a transient source detected in October 2017 by INTEGRAL. The absence of eclipse in the light curve suggests an inclination smaller than 75º. With this inclination, and assuming a 1.4 $M_\odot$ NS, the companion mass is greater than 0.0065 $M_\odot$. The magnetic field is in the range $9.2 \cdot 10^8$ - $5.2 \cdot 10^{10}$ G [22].

### 3.3.12 IGR J17062−6143

IGR J17062−6143 is an AMXP in a compact binary system ($P_{orb} \sim 38$ minutes) discovered during an outburst in 2006. It presents long thermonuclear X-ray bursts compatible with a degenerate He dwarf companion [23]. Nevertheless, in 2018, another work suggested the surrounding is rich in oxygen and the donor could be a CO or a O-Ne-Mg white dwraf [24].

Table III: Sample of the studied AMXPs

| Source name | Coordinates RA (J2000) / DEC (J2000) | Pulse period (ms) | Orbital period (h) | Distance (kpc) | Distance chosen (kpc) |
|---|---|---|---|---|---|
| Swift J1756.9−2508 | $17^h56^m57^s.35$ / - 25°06'27".8 | 5.5[1] | 0.9117[1] | 8.5[1] | 8.5[1] |
| IGR J17591−2342 | $17^h59^m08^s.79$ / - 23°42'46".7 | 1.9[2] | 8.8013[2] | $7.6^{+0.7}_{-0.7}$ [2] | 7.6 |
| IGR J00291+5934 | $00^h29^m03^s.06$ / 59°34'19".0 | 1.7[3] | 2.4567[3] | 2-4[4] | 3 |
| IGR J1737.9−3747 | $17^h37^m58^s.80$ / - 37°46'19".2 | 2.1[5] | 1.8794[5] | $\sim 8.5$[5] | 8.5 |
| IGR J17511−3057 | $17^h51^m08^s.55$ / - 30°57'41".7 | 4.1[6] | 3.4688[6] | $< 6.9$[7] | 6.9[6] |
| MAXI J0911−655 | $09^h12^m02^s.43$ / - 64°52'06".4 | 2.9[8] | 0.7389[8] | $9.45^{+0.13}_{-0.15}$ [9] | 9.5[8] |
| PSR J1023+0038 | $10^h23^m47^s.68$ / 00°38'41".0 | 1.69[10] | 4.7543[10] | $1.368^{+0.042}_{-0.039}$ [10] | 1.37 |
| SAX J1748.9−2021 | $17^h48^m52^s.16$ / - 20°21'32".4 | 2.3[11] | 8.7653[11] | $8.1^{+1.3}_{-1.3}$ [12] | 8.5[11] |
| SAX J1808.4−3658 | $18^h08^m27^s.54$ / - 36°58'44".3 | 2.5[13] | 2.0136[13] | 3.4-3.6 [14] | 3.5 |
| Swift J1749.4−2807 | $17^h49^m31^s.94$ / - 28°08'05".8 | 1.9[15] | 8.8169[15] | $6.7^{+1.3}_{-1.3}$ [15] | 7 |
| IGR J16597−3704 | $16^h59^m32^s.90$ / - 37°07'14".3 | 9.5[16] | 0.7661[16] | 9.1[17] | 9.1 |
| IGR J17062−6143 | $17^h06^m16^s.29$ / - 61°42'40".6 | 6.1[18] | 0.6328[18] | $7.3^{+0.5}_{-0.5}$ [19] | 7.3[18] |

Coordinates resolved by SIMBAD (1) Estimate from the direction of the galactic center [9] (2) [25] (3) [26] (4) [11] (5) Distance unknown precisely. Estimate from the direction of the galactic center [13] (6) [14] (7) [27] (8) [15] (9) Distance of the cluster NGC 2808 [28] (10) [29] (11) [18] (12) [30] (13) [31] (14) [32] (15) [33] (16) [22] (17) Distance of cluster NGC 6256 [34] (18) [23] (19) [35]

# 4 Results and discussion

The spectral fits obtained with XSPEC version 12.11.1 for each source are reported here. The COMPPS continuum model was modified with the absorption component TBABS and a constant was added to take into account different normalisations of the data from different observatories. The final model in XSPEC is CONST*TBABS*COMPPS. The constant is fixed at 1 for the FPMA NuSTAR data and kept free for the other ones. The TBABS component has a free hydrogen column density parameter ($N_{\rm H}$). The parameters of the COMPPS model are presented in table I.

For a given observation, there are 2 plots corresponding to the different redshifts. The redshift fixed at 0 is showen on the left and the same parameter fixed at 0.26

on the right. The value for each free parameter is reported in tables IV and V. For few sources, I added a DISKBB component to the COMPPS model when the latter alone did not allow to obtain a reasonable fit. In those cases, the parameters values are reported in tables VI and VII.

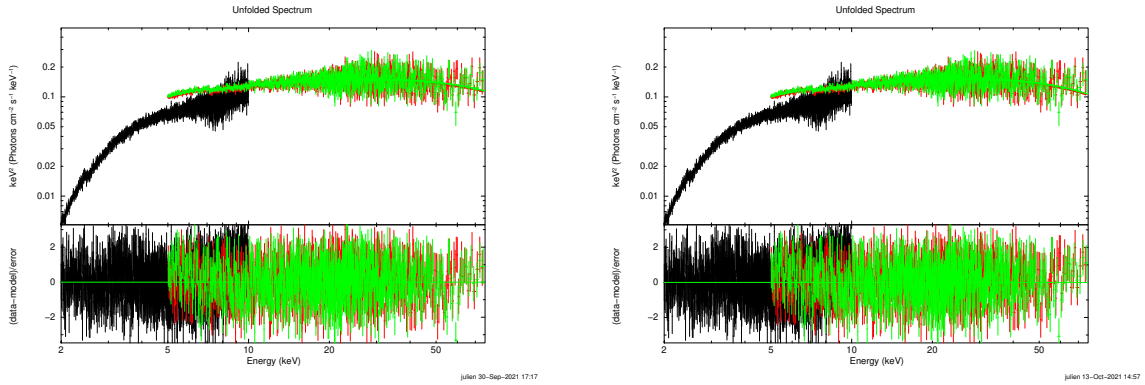


Figure 5: Swift J1756.9−2508 2018 / Soft = XMM-Newton / Energy range: 2-10 keV for MOS and 5-78 keV for NuSTAR / COMPPS, $z = 0$ (left) and $z = 0.26$ (right).

## 4.1 Results by source

### 4.1.1 Swift J1756.9−2508

NuSTAR observed this source 2 times, in 2018 and 2019. In 2021, Li et al. [36] analysed these observations. They used the same model as me, but their energy band was broader (they used INTEGRAL-ISGRI data for the hard band and NICER data for the soft X-ray band). For the 2018 data (Figure 5), I used the simultaneous XMM-Newton MOS observation as soft one. The XMM-Newton data below 2 keV were ignored as well as the NuSTAR data between 3 and 5 keV. I found $N_{\rm H} = 6.16^{+0.13}_{-0.13} \times 10^{22}$ cm$^{-2}$ , $kT_{\rm bb} = 0.87^{+0.02}_{-0.02}$ keV and $kT_{\rm e} = 32.0^{+1.0}_{-1.0}$ keV. Li et al. found $N_{\rm H} = 4.29^{+0.05}_{-0.05} \times 10^{22}$ cm$^{-2}$ , $kT_{\rm bb} = 0.79^{+0.01}_{-0.01}$ keV and $kT_{\rm e} = 41.6^{+0.7}_{-0.7}$ keV.

For the 2019 observation (Figure 6), a Swift/XRT observation was done one day after NuSTAR. All the available data were used. I found $N_{\rm H} = 4.24^{+0.92}_{-0.59} \times 10^{22}$ cm$^{-2}$ , $kT_{\rm bb} = 0.81^{+0.05}_{-0.06}$ keV and $kT_{\rm e} = 38.1^{+1.6}_{-1.5}$ keV. Li et al. found $N_{\rm H} = 4.17^{+0.12}_{-0.12} \times 10^{22}$ cm$^{-2}$, $kT_{\rm bb} = 0.67^{+0.02}_{-0.02}$ keV and $kT_{\rm e} = 44.6^{+1.3}_{-1.3}$ keV.

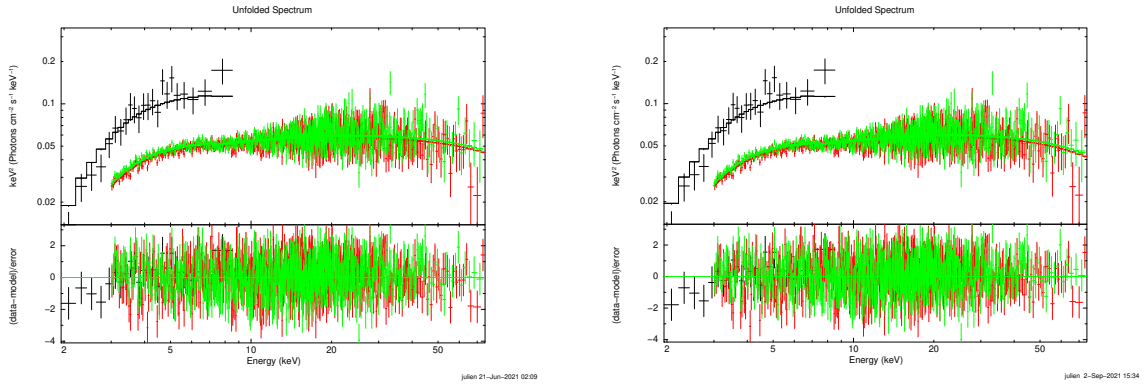


Figure 6: Swift J1756.9−2508 2019 / Soft = Swift/XRT / Energy range: 0.5-10 keV for XRT and 3-78 keV for NuSTAR / COMPPS, $z = 0$ (left) and $z = 0.26$ (right).

### 4.1.2 IGR J17591−2342

In August 2018, NuSTAR observed the source two times in 4 days. 2 different Swift/XRT observations were performed one day after each NuSTAR observation. For the first observation ($13^{th}$ August), all the data available were used (0.5-10 keV for XRT and 3-78 keV for NuSTAR). I reduced the XRT observations with the XRT pipeline (Figure 7). The results are consistent with those obtained by Kuiper et al. in 2020 [25].

For the second NuSTAR observation done on $17^{th}$ August (ID = 80301311002), errors occured when the energies below 3 keV are used from Swift/XRT data. The parameters values were significantly different and poorly constrained compared to the precedent observation or to the results obtained by Kuiper et al.. Following that, like Kuiper et al. did, I fitted this observation with the XMM-Newton data performed about 2 weeks after NuSTAR on $3^{rd}$ September (Figure 8).

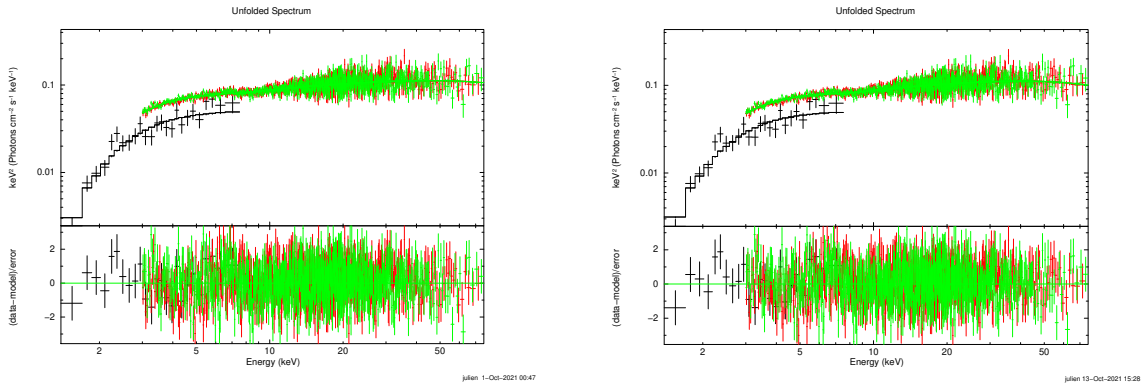


Figure 7: IGR J17591−2342 $13^{th}$ August 2018 / Soft = Swift/XRT / Energy range: 0.5-10 keV for XRT and 3-78 keV for NuSTAR / COMPPS, $z = 0$ (left) and $z = 0.26$ (right).

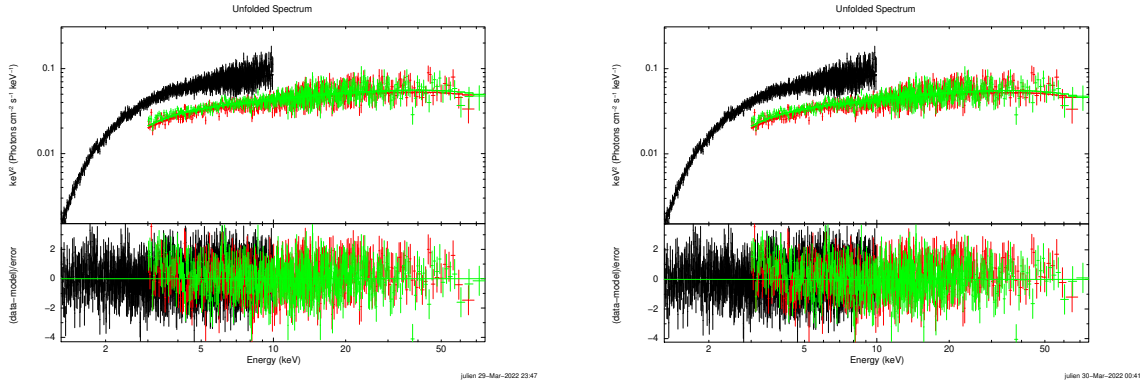


Figure 8: IGR J17591−2342 $17^{th}$ August 2018 / Soft = XMM-Newton / Energy range: 1.3-10 keV for MOS and 3-78 keV for NuSTAR / COMPPS, $z = 0$ (left) and $z = 0.26$ (right).

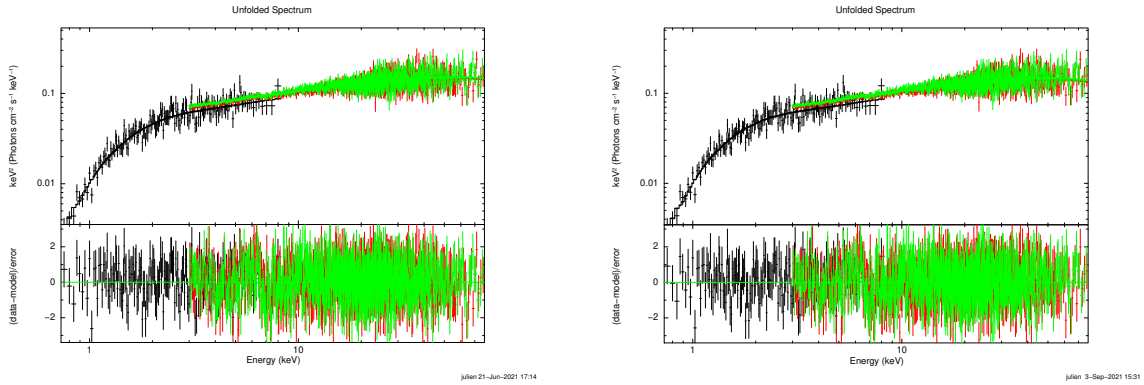


Figure 9: IGR J00291+5934 / Soft data = Swift/XRT / Energy range: 0.7-10 keV for XRT and 3-78 keV for NuSTAR / COMPPS, $z = 0$ (left) and $z = 0.26$ (right).

### 4.1.3 IGR J00291+5934

NuSTAR observed the source one day before Swift in July 2015. All the parameters are constrained by combining the both observations (Figure 9). All the data available were used (0.7-10 keV for XRT WT and 3-78 keV for NuSTAR). In their work, Sanna et al. [37] fitted this NuSTAR observation by using an XMM-Newton one for soft data. The model was TBABS*(GAUSSIAN+GAUSSIAN+BBODY+NTHCOMP). The gaussian lines are at 6.47 and 2.24 keV, they fixed the $N_{\rm H}$ and $kT_{\rm e}$ parameters at $0.226 \times 10^{22}$ cm$^{-2}$ and 28.8 keV respectively. I found $N_{\rm H} = 0.44^{+0.06}_{-0.05} \times 10^{22}$ cm$^{-2}$ and $kT_{\rm e} = 44.5^{+2.4}_{-1.9}$ keV.

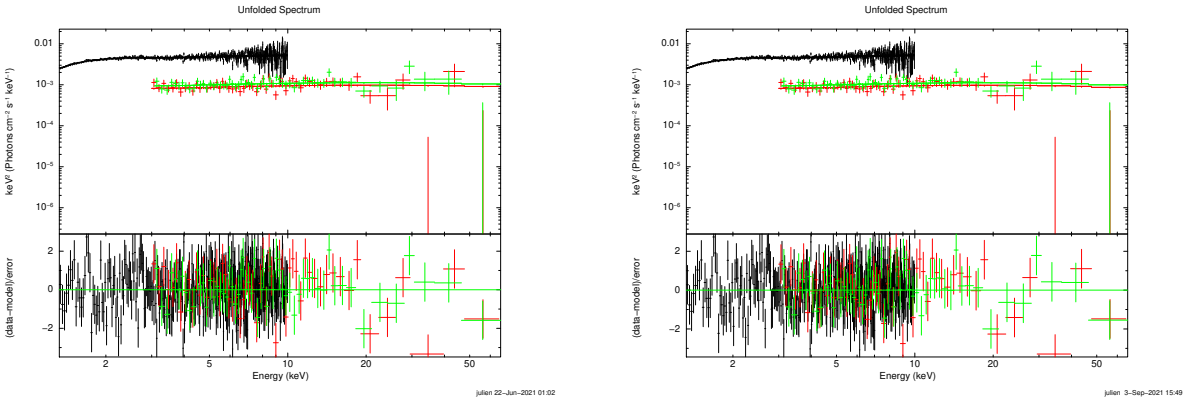


Figure 10: IGR J1737.9−3747 / Soft = XMM-Newton / Energy range: 1.3-10 keV for PN 3-78 keV for NuSTAR / COMPPS, $z = 0$ (left) and $z = 0.26$ (right).

### 4.1.4 IGR J1737.9−3747

XMM-Newton observed this source one day before NuSTAR in 2018. The MOS data is not available for an online analysis on the XMM-Newton archive website. Then, I used the PN observation (reduced by using SAS). The energy range selected was 1.3-10 keV for XMM-Newton and 3-78 keV for NuSTAR. Swift/XRT observed it the same day as NuSTAR, but the spectrum does not allow to fit the data. The COMPPS model allows to constrain all the parameters (Figure 10). Sanna et al. in 2018 [38] analysed the XMM-Newton observation. The model used was CONST × TBABS × [DISKBB + NTHCOMP]. The electron temperature $kT_{\rm e}$ was fixed at 30 keV. I found $kT_{\rm e} = 57.2^{+4.1}_{-4.0}$ keV by using a larger energy band than Sanna et al.. The luminosity of this source is about $10^{35}$ erg s$^{-1}$.

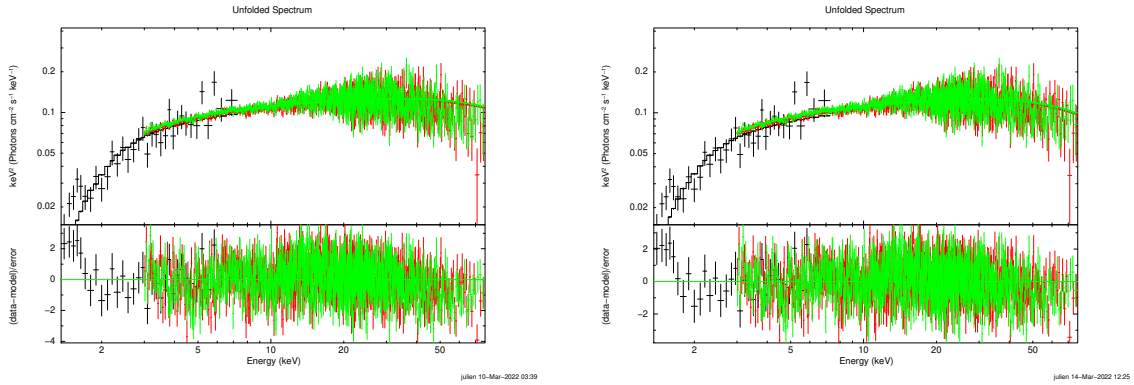


Figure 11: IGR J17511−3057 / Soft = Swift/XRT / Energy range: 1.3-10 XRT, 3-78 keV NuSTAR / COMPPS, $z = 0$ (left) and $z = 0.26$ (right).

### 4.1.5 IGR J17511−3057

NuSTAR observed this source on $8^{th}$ April 2015. A Swift/XRT observation was performed on the same day. I used the soft data between 1.3 and 10 keV (Figure 11). The optical depth parameter $\tau$ was fixed at 1.5 for this source because it was impossible to constrain it at some meaningful value.

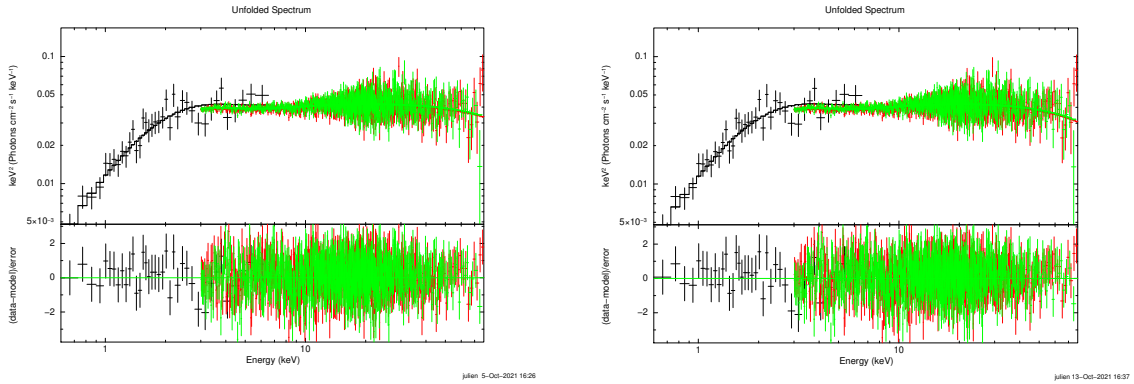


(a) obs 90201024002 May 2016

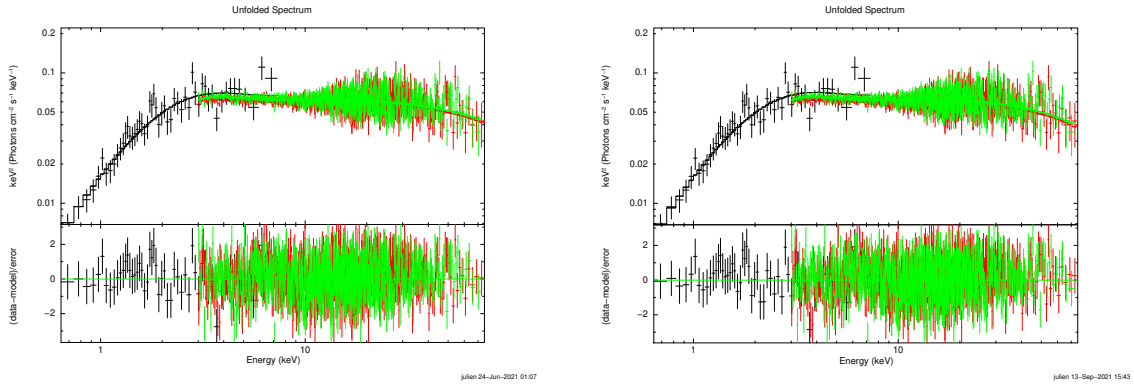


(b) obs 90201042002 November 2016

Figure 12: MAXI J0911−655 / Soft = Swift/XRT / Energy range: 0.5-10 keV Swift/XRT 3-78 keV NuSTAR / COMPPS, $z = 0$ (left) and $z = 0.26$ (right).

### 4.1.6 MAXI J0911−655

NuSTAR observed this source 2 times in 2016 (in May and in November). Two Swift observations did the same day as NuSTAR were used to get the soft data (Figure 12). All the data available were used. The hydrogen column density is not constrained in both observations. The 3 $\sigma$ upper limit is smaller with a redshift fixed at 0 ($N_{\rm H} < 0.1\ 10^{22}$ cm$^{-2}$ for $z = 0$ and $N_{\rm H} < 1.5\ 10^{22}$ cm$^{-2}$ for $z = 0.26$).

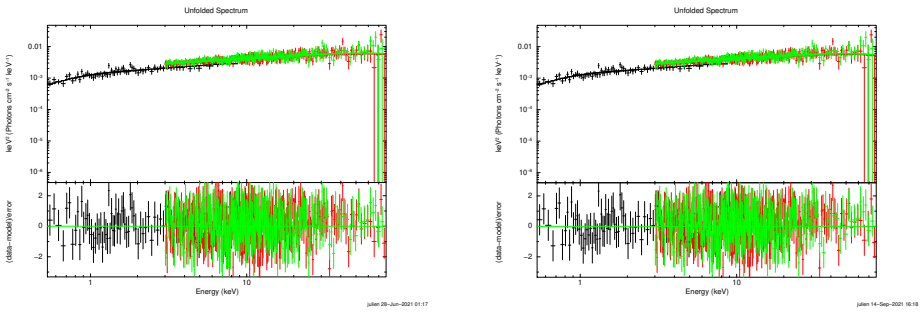


Figure 13: PSR J1023+0038 October 2013 / Soft data = Swift/XRT / Energy range: 0.5-10 keV for Soft data and 3-78 keV for NuSTAR / COMPPS, $z = 0$ (left) and $z = 0.26$ (right).

### 4.1.7 PSR J1023+0038

There are 6 NuSTAR observations between June 2013 and 2018. This source was in a LMXB state from October 2013 to 2019. During this phase, it presented different X-ray states [6]. The NuSTAR observations between October 2013 and 2017 were done during a high luminosity mode ($L \sim 7 \times 10^{33}$ erg s$^{-1}$). In June 2013 (two observations) PSR J1023+0038 was in a MSP state ($L \sim 10^{32}$ erg s$^{-1}$), so these observations are not in the sample.

In October 2013 (Figure 13), a Swift observation was done a day before the NuSTAR one. In May 2016 (Figure 14), Swift observed the source simultaneously with NuSTAR. In June 2017 (Figure 16), the source was observed by Swift one day after NuSTAR. For these observations, the Swift data were used in soft band. For the observation done in May 2017 (Figure 15), XMM-Newton observed the source simultaneously with NuSTAR as well as Swift. The XMM-Newton data were used to fit the data since it has much better statistics. In all cases, all the data available were used and the hydrogen column density parameter cannot be constrained by the model ($N_{\rm H} < 1.5\ 10^{22}$ cm$^{-2}$ ).

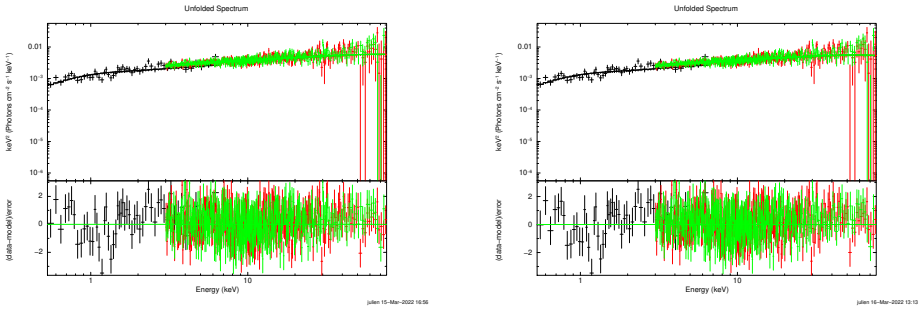


Figure 14: PSR J1023+0038 May 2016 / Soft = Swift/XRT / Energy range: 0.5-10 keV for XRT and 3-78 keV for NuSTAR / COMPPS, $z = 0$ (left) and $z = 0.26$ (right).

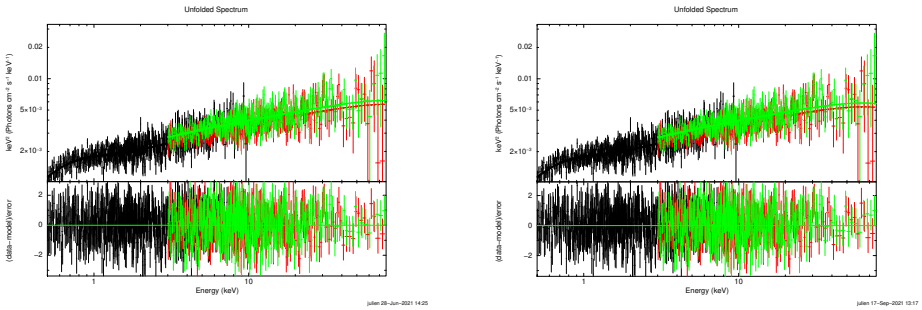


Figure 15: PSR J1023+0038 May 2017 / Soft = XMM-Newton / Energy range: 0.5-10 keV for MOS and 3-78 keV for NuSTAR / COMPPS, $z = 0$ (left) and $z = 0.26$ (right).

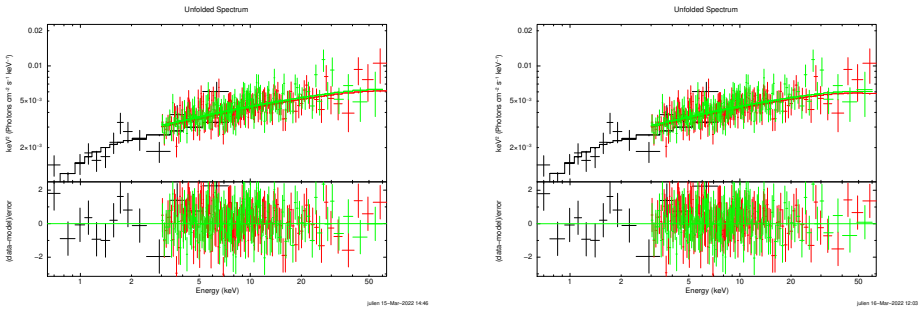


Figure 16: PSR J1023+0038 June 2017 / Soft data = Swift/XRT / Energy range: 0.5-10 keV for XRT and 3-78 keV for NuSTAR / COMPPS, $z = 0$ (left) and $z = 0.26$ (right).

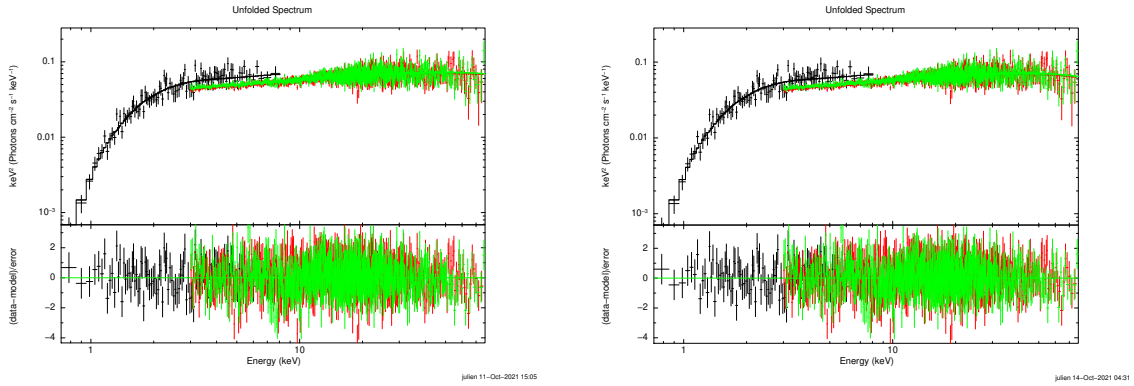


Figure 17: SAX J1748.9−2021 in 2017 / Soft = Swift/XRT / Energy range: 0.7-10 keV for XRT and 3-78 keV for NuSTAR / COMPPS, $z = 0$ (left) and $z = 0.26$ (right).

### 4.1.8 SAX J1748.9−2021

There are two observations for this source: One in 2015 and another one in 2017. For the 2017 observation (Figure 17), the Swift data allows to get a good fit together with the NuSTAR data.

I did not include the 2015 observation in the sample. In fact, the best fit obtained presented issues with unusual parameters value (for example, the normalisation parameter was about $10^7$ km$^2$). In the literature, Pintore et al. in 2016 [39] modelled the 2015 XMM-Newton and INTEGRAL observations of this source. They found the source had an high X-ray burst activity which affected the persistent emission. They used a POWER-LAW and 6 GAUSSIAN components in addition to a DISKBB and a NTHCOMP component to be able to model the data.

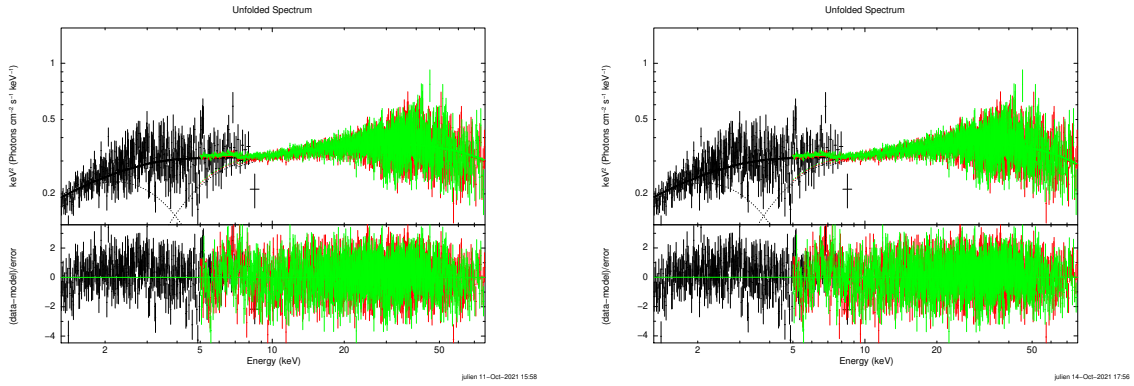


Figure 18: SAX J1808.4−3658 April 2015 / Soft data = Swift/XRT / Energy range: 0.7-10 keV for XRT and 3-78 keV for NuSTAR / COMPPS + DISKBB, $z = 0$ (left) and $z = 0.26$ (right).

### 4.1.9 SAX J1808.4−3658

Three observations done by NuSTAR are available. In April, May 2015 and in 2019. In April 2015, it is not possible to fit well the data by using the XRT observation done the same day as the NuSTAR one without the DISKBB component. In fact, residuals appear between 3 and 10 keV due to the reflection component. In 2019, Di Salvo et al. [40] also modelled this observation by using a DISKBB component. The data below 1.3 keV were ignored (Figure 18).

For the other observations (May 2015 and 2019, respectively Figures 19 and 20), a simultaneous Swift observation with NuSTAR is available and a DISKBB component is not needed to obtain a good fit. The COMPPS model is not able to constrain the hydrogen column density parameter. Moreover, due to residuals in this energy range, the Swift/XRT data between 8 and 10 keV were ignored for the observation done in 2019.

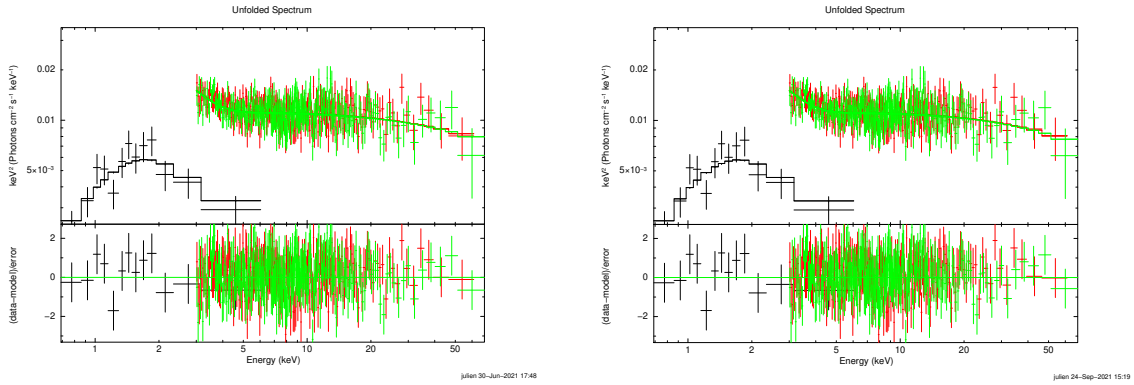


Figure 19: SAX J1808.4−3658 May 2015 / Soft = Swift/XRT / Energy range: 0.5-10 keV for XRT and 3-78 keV for NuSTAR / COMPPS, $z = 0$ (left) and $z = 0.26$ (right).

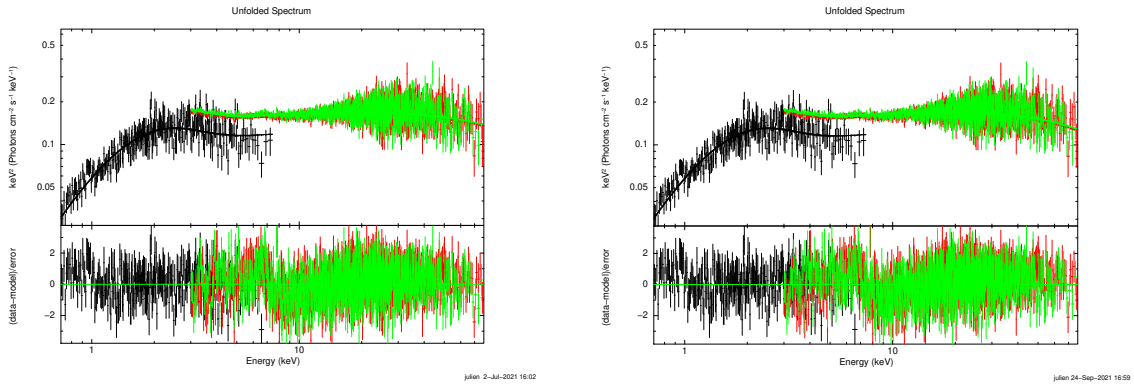


Figure 20: SAX J1808.4−3658 August 2019 / Soft = Swift/XRT / Energy range: 0.7-8 keV for XRT and 3-78 keV for NuSTAR / COMPPS, $z = 0$ (left) and $z = 0.26$ (right).

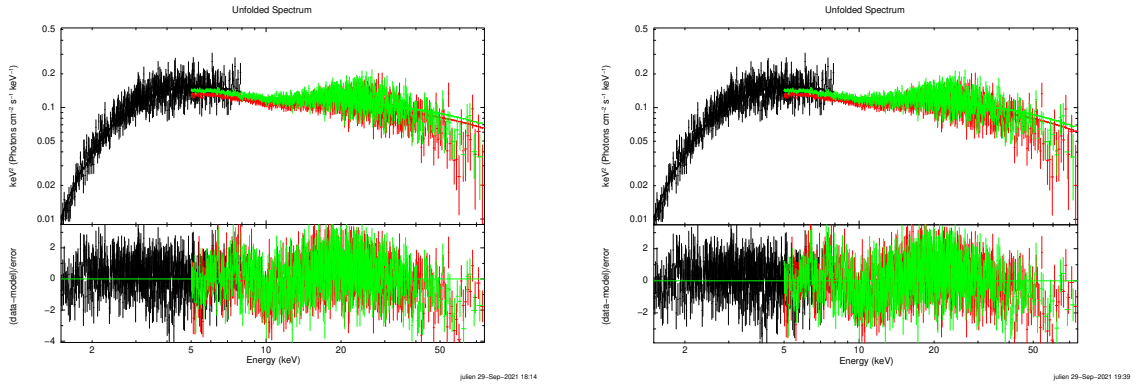


Figure 21: Swift J1749.4−2807 / Soft = XMM-Newton / Energy range: 1.5-8 keV for MOS and 5-78 keV for NuSTAR / COMPPS, $z = 0$ (left) and $z = 0.26$ (right).

### 4.1.10 Swift J1749.4−2807

XMM-Newton observed this source on the same day as NuSTAR, on $4^{th}$ March 2021. Swift observed the source one month later, then I used the XMM-Newton data (Figure 21). The COMPPS model allows to constrain all the parameters. Some energies range have been ignored: energies below 1.5 keV and above 8 keV for XMM-Newton and below 5 keV for NuSTAR.

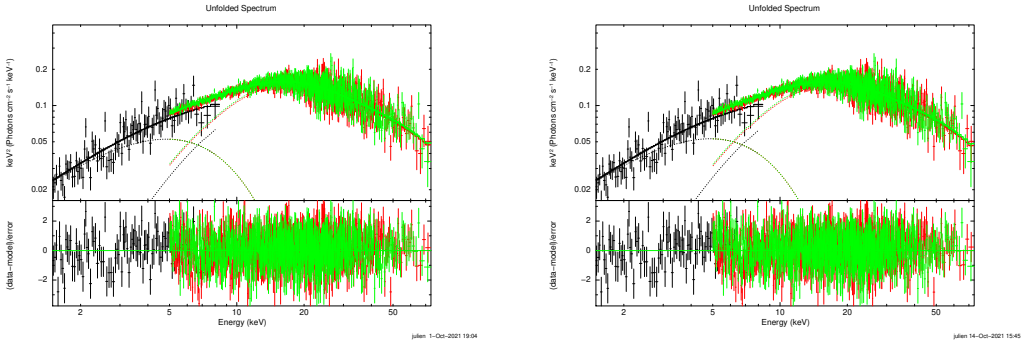


Figure 22: IGR J16597−3704 / Soft: Swift/XRT / Energy range: 1.5-10 keV for XRT-WT 5-78 keV for NuSTAR / COMPPS + DISKBB, $z = 0$ (left) and $z = 0.26$ (right).

### 4.1.11 IGR J16597−3704

For this source, I used a Swift/XRT observation done one day before NuSTAR for fitting the soft X-ray band. Because the COMPPS model does not allow to obtain a good fit, I added a DISKBB component to improve the fit quality (this component was also used by Sanna et al. in 2018 [22]). The NuSTAR data between 3 and 5 keV were ignored. A better model is obtained by reducing the XRT data with XRT pipeline instead of taking the online reduced ones. Energies below 1.5 keV were ignored for the XRT data (Figure 22).

### 4.1.12 IGR J17062−6143

NuSTAR observed this source two times: in 2015 and 2016. The DISKBB component is needed to improve the models. In fact, some deviations around 10 keV and up to 30 keV are visible with the COMPPS model alone. When they analysed these data in 2018, Eijnden et al. [41] also needed to include a DISKLINE component to their model. They added a gaussian line I did not include in mine. For both observations, a simultaneous Swift observation were available. In 2015 (Figure 23a), the hydrogen column density parameter is not constrained. The data below 0.8 keV are ignored for the XRT observation. I got a similar value for the soft photons temperature as Eijnden et al.. In 2016 (Figure 23b), there are different parameters values compared to the precedent observation. In fact, the soft photons temperature value is high compared to the 2015 observation and to the Eijnden model in 2017. It is also the case for the hydrogen column density from the TBABS component.

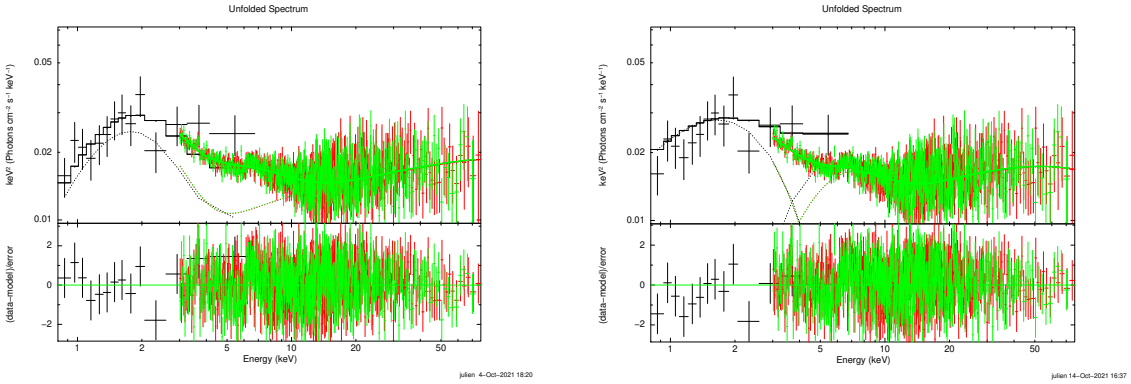


(a) Observation 30101034002 (2015) / Energy range: 0.8-10 for XRT, 3-78 keV for NuSTAR.

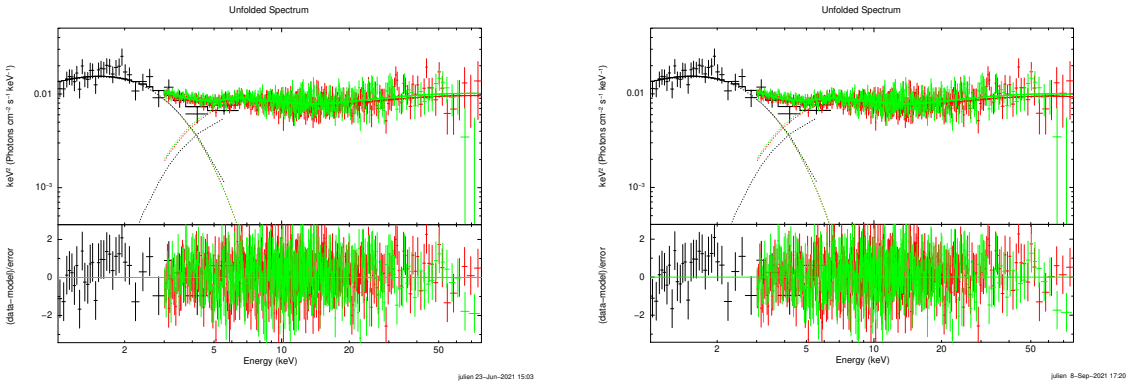


(b) Observation 30201018002 (2016) / Energy range: 1.0-10 for XRT, 3-78 keV for NuSTAR.

Figure 23: IGR J17062−6143 / Soft data = Swift XRT / COMPPS + DISKBB, $z$ = 0 (left) and $z = 0.26$ (right).

## 4.2 Discussion

### 4.2.1 Parameters value

The COMPPS model allows to obtain an acceptable fit for most of the AMXPs from our sample. Then, it is possible to perform a comparative analysis of the parameters values obtained for the different sources (Figure 24). To have as homogeneous sample as possible we excluded 3 sources required a DISKBB component (see Tables VI and VII). Moreover, we did not include in the sample the observations performed when the transitional millisecond pulsar PSR J1023+0038 was not in an accreting mode, before October 2013.

The electron temperature ($kT_{\rm e}$) for SAX J1808.4−3658 (green point) is not well constrained by the model and high compared with the other sources. Here, the model has probably overestimated the temperature. In fact, 3 weeks before this observation, NuSTAR did another one where the electron temperature I found was similar to the value found in [40]: $38.3^{+1.4}_{-1.1}$ keV. By ignoring this point, there is no source with a noticeable different value and the whole sample of sources does not demonstrate strong correlation of $kT_e$ with the luminosity: This temperature is about 40-60 keV for the sample regardless the luminosity.

The seed photons temperature ($kT_{\rm bb}$) shows positive correlation with the luminosity both considering the whole sample and individual sources. As can be seen from the plot, $kT_{\rm bb}$ increases with the luminosity of the source. For instance, one can see a significant increase of the temperature between PSR J1023+0038 (red points in low luminosity), and Swift J1749.4−2807 (brown point).

The hydrogen column density $N_{\rm H}$ is the least constrained parameter: 3 sources have their hydrogen column density not constrained. From left to right on figure 24: PSR J1023+0038 (red points), SAX J1808.4−3658 (green points) and MAXI

J0911−655 (grey points). On the whole, it does not show significant variations. The vertical optical depth of the corona $\tau$ is most of the time smaller than 1.5 which indicate a reasonable result as indicated in the XSPEC manual. When this parameter was largely higher than 1.5 and poorly constrained, I fixed it at 1.5. It is indicated in Tables VI and VII.

The normalisation parameter $K$ does not show a significant variation with the luminosity. It is expected as the normalisation value is linked to the source radius and the distance. From the $K$ parameter, the COMPPS model allows to estimate the source radius $r$:

$$r \sim D_{10} \sqrt{K}, \tag{11}$$

where $D_{10}$ is the distance to the source in unit of 10 kpc and $r$ in km. I calculated the source radius estimated by the model with the distances taken from Table III. The result is also reported on Figure 24. The radius is underestimated for the sources with low luminosity. Especially for PSR J1023+0038 (red points in low luminosity). The radius estimated for IGR J17511−3057 (yellow point) is about 22 km, which is too high. This error could come from the distance which is not well known for IGR J17511−3057 [27].

Most of the sources have a luminosity about $10^{36}$ erg s$^{-1}$. PSR J1023+0038 (red points), have a lower luminosity ($10^{33}$ - $10^{34}$ erg s$^{-1}$) which is coherent with a transitional X-ray millisecond pulsar in an AMXP phase [42]. IGR J1737.9−3747 (pink point) declined in luminosity in early April 2018 when it was observed by NuSTAR [43].

Table IV: Spectral parameters: Model = TBABS*COMPPS ; redshift fixed at 0

| Source | obs ID NuSTAR | Date NuSTAR (YMD) | obs ID Soft | Date Soft (YMD) | Energy range (keV) | $N_{\rm H}$ ($10^{22}$ cm$^{-2}$) | $kT_{\rm bb}$ (keV) | $kT_{\rm e}$ (keV) | $\tau$ | $K$ (km$^2$) | Flux[1] ($10^{-10}$ erg s$^{-1}$ cm$^{-2}$) | Luminosity ($10^{36}$ erg s$^{-1}$) | C-value (dof) | Figure |
|---|---|---|---|---|---|---|---|---|---|---|---|---|---|---|
| Swift J1756.9−2508 | 90402313002 | 18-04-08 | 0830190401 (N) | 18-04-08 (N) | 2-10 MOS 5-78 NS | $6.16^{+0.13}_{-0.13}$ | $0.87^{+0.02}_{-0.02}$ | $32.0^{+1.0}_{-1.0}$ | $1.76^{+0.04}_{-0.04}$ | $103^{+10}_{-9}$ | 6.983 | 6.038 | 3048.38 (2878) | 5 |
| Swift J1756.9−2508 | 90501329001 | 19-06-22 | 00030952025 (S) | 19-06-21 (S) | 0.5-10 XRT 3-78 NS | $4.24^{+0.92}_{-0.59}$ | $0.81^{+0.05}_{-0.06}$ | $38.1^{+1.6}_{-1.5}$ | $1.45^{+0.05}_{-0.05}$ | $58^{+23}_{-12}$ | 2.924 | 2.528 | 1279.8 (1209) | 6 |
| IGR J17591−2342 | 90401331002 | 18-08-13 | 00010804002 (S) | 18-08-14 (S) | 0.5-10 XRT 3-78 NS | $3.01^{+0.45}_{-0.39}$ | $0.76^{+0.04}_{-0.04}$ | $47.4^{+1.7}_{-1.7}$ | $1.35^{+0.04}_{-0.04}$ | $118^{+28}_{-20}$ | 5.539 | 3.829 | 1292.46 (1269) | 7 |
| IGR J17591−2342 | 80301311002 | 18-08-17 | 0795750101 (N) | 18-09-03 (N) | 1.3-10 MOS 3-78 NS | $2.87^{+0.06}_{-0.06}$ | $0.65^{+0.02}_{-0.02}$ | $33.4^{+1.9}_{-1.9}$ | $1.87^{+0.08}_{-0.07}$ | $94^{+13}_{-11}$ | 2.520 | 1.742 | 2384.7 (2286) | 8 |
| IGR J00291+5934 | 90101010002 | 15-07-28 | 00031258006 (S) | 15-07-29 (S) | 0.7-10 XRT-WT 3-78 NS | $0.44^{+0.06}_{-0.05}$ | $0.47^{+0.02}_{-0.03}$ | $44.5^{+2.4}_{-1.9}$ | $1.59^{+0.05}_{-0.06}$ | $797^{+181}_{-126}$ | 7.321 | 0.789 | 1674.88 (1739) | 9 |
| IGR J1737.9−3747 | 90401312002 | 18-04-02 | 0830190301 (N) | 18-04-01 (N) | 1.3-10 PN 3-78 NS | $0.72^{+0.12}_{-0.10}$ | $0.35^{+0.02}_{-0.02}$ | $57.2^{+4.1}_{-4.0}$ | $0.97^{+0.06}_{-0.06}$ | $26.7^{+7.7}_{-5.2}$ | 0.06252 | 0.05406 | 494.9 (455) | 10 |
| IGR J17511−3057 | 90101001002 | 15-04-08 | 00031492033 (S) | 15-04-08 (S) | 1.3-10 XRT 3-78 NS | $2.54^{+0.12}_{-0.12}$ | $0.45^{+0.02}_{-0.02}$ | $40.4^{+0.2}_{-0.2}$ | 1.5[2] | $1083^{+189}_{-166}$ | 6.587 | 3.753 | 1817 (1593) | 11 |
| MAXI J0911−655 | 90201024002 | 16-05-24 | 00081952001 (S) | 16-05-24 (S) | 0.5-10 XRT 3-78 NS | $< 0.1$ [*] | $0.58^{+0.02}_{-0.02}$ | $46.7^{+0.9}_{-1.0}$ | $1.18^{+0.02}_{-0.02}$ | $159^{+21}_{-17}$ | 2.694 | 2.910 | 1210.68 (1311) | 12 |
| MAXI J0911−655 | 90201042002 | 16-11-23 | 00088013001 (S) | 16-11-23 (S) | 0.5-10 XRT 3-78 NS | $< 0.1$ [*] | $0.64^{+0.01}_{-0.02}$ | $42.0^{+1.0}_{-1.0}$ | $1.20^{+0.02}_{-0.02}$ | $176^{+24}_{-14}$ | 3.887 | 4.198 | 1199.56 (1215) | 12 |
| PSR J1023+0038 | 30001027006 | 13-10-19 | 00080035003 (S) | 13-10-18 (S) | 0.5-10 XRT 3-78 NS | $< 1.5$ [*] | $0.22^{+0.03}_{-0.04}$ | $40.7^{+6.5}_{-7.5}$ | $1.78^{+0.29}_{-0.21}$ | $464^{+377}_{-154}$ | 0.3141 | 0.007055 | 800.55 (765) | 13 |
| PSR J1023+0038 | 30201005002 | 16-05-07 | 00092401001 (S) | 16-05-08 (S) | 0.5-10 XRT 3-78 NS | $< 1.5$ [*] | $0.24^{+0.04}_{-0.05}$ | $50.7^{+1.4}_{-1.1}$ | 1.5[2] | $321^{+419}_{-130}$ | 0.2991 | 0.006718 | 740.89 (744) | 14 |
| PSR J1023+0038 | 80201028002 | 17-05-23 | 0794580801 (N) | 17-05-23 (N) | 0.5-10 MOS 3-78 NS | $< 1.5$ [*] | $0.17^{+0.01}_{-0.01}$ | $62.0^{+2.8}_{-2.8}$ | $1.25^{+0.05}_{-0.04}$ | $1265^{+231}_{-178}$ | 0.2950 | 0.006626 | 1175.2 (1176) | 15 |
| PSR J1023+0038 | 90301006002 | 17-06-13 | 00033012166 (S) | 17-06-13 (S) | 0.5-10 XRT 3-78 NS | $< 1.5$ [*] | $0.30^{+0.04}_{-0.05}$ | $47.9^{+1.5}_{-1.4}$ | 1.5[2] | $167^{+148}_{-66}$ | 0.3302 | 0.007417 | 267.46 (285) | 16 |
| SAX J1748.9−2021 | 90301320002 | 17-10-11 | 00010341005 (S) | 17-10-11 (S) | 0.7-10 XRT-WT 3-78 NS | $1.02^{+0.11}_{-0.10}$ | $0.59^{+0.02}_{-0.02}$ | $52.4^{+2.3}_{-1.9}$ | $1.23^{+0.04}_{-0.03}$ | $259^{+48}_{-37}$ | 3.797 | 3.283 | 1369.20 (1433) | 17 |
| SAX J1808.4−3658 | 90102003004 | 15-05-09 | 00030034088 (S) | 15-05-09 (S) | 0.5-10 XRT 3-78 NS | $< 0.4$ [*] | $0.39^{+0.02}_{-0.02}$ | $79.6^{+10.1}_{-6.1}$ | $0.49^{+0.06}_{-0.09}$ | $321^{+135}_{-65}$ | 0.9937 | 0.1457 | 413.83 (484) | 19 |
| SAX J1808.4−3658 | 90501335002 | 19-08-10 | 00033801025 (S) | 19-08-09 (S) | 0.7-8 XRT 3-78 NS | $< 1.5$ [*] | $0.47^{+0.01}_{-0.01}$ | $56.8^{+0.9}_{-0.8}$ | $0.93^{+0.02}_{-0.02}$ | $1565^{+78}_{-73}$ | 11.85 | 1.737 | 2032.48 (1901) | 20 |
| Swift J1749.4−2807 | 90701310002 | 21-03-04 | 0872392001 (N) | 21-03-04 (N) | 1.5-8 MOS 5-78 NS | $2.58^{+0.10}_{-0.10}$ | $0.89^{+0.01}_{-0.01}$ | $45.4^{+0.8}_{-0.8}$ | $0.98^{+0.02}_{-0.01}$ | $96.7^{+7.0}_{-6.5}$ | 6.186 | 3.628 | 2225.48 (1842) | 21 |

(N) XMM-Newton (S) Swift/XRT (*) Upper limit 3 $\sigma$ (1) Unabsorbed flux in the 0.5 – 100 keV energy range (2) Parameter frozen

Table V: Spectral parameters: Model = TBABS*COMPPS ; redshift fixed at 0.26 (10)

| Source | obs ID NuSTAR | Date NuSTAR (YMD) | obs ID Soft | Date Soft (YMD) | Energy range (keV) | $N_{\rm H}$ ($10^{22}$ cm$^{-2}$) | $kT_{\rm bb}$ (keV) | $kT_{\rm e}$ (keV) | $\tau$ | $K$ (km$^2$) | Flux [1] ($10^{-10}$ erg s$^{-1}$ cm$^{-2}$) | Luminosity ($10^{36}$ erg s$^{-1}$) | C-value (dof) | Figure |
|---|---|---|---|---|---|---|---|---|---|---|---|---|---|---|
| Swift J1756.9−2508 | 90402313002 | 18-04-08 | 0830190401 (N) | 18-04-08 (N) | 0.5-10 MOS 5-78 NS | $6.03^{+0.12}_{-0.12}$ | $1.13^{+0.02}_{-0.02}$ | $35.5^{+0.9}_{-0.9}$ | $1.65^{+0.03}_{-0.03}$ | $56.5^{+4.7}_{-4.1}$ | 6.912 | 5.976 | 3054.34 (2878) | 5 |
| Swift J1756.9−2508 | 90501329001 | 19-06-22 | 00030952025 (S) | 19-06-21 (S) | 0.5-10 XRT 3-78 NS | $3.88^{+0.41}_{-0.66}$ | $1.06^{+0.06}_{-0.06}$ | $40.5^{+1.4}_{-1.4}$ | $1.40^{+0.04}_{-0.04}$ | $30.4^{+8.7}_{-5.7}$ | 2.895 | 2.503 | 1278.58 (1209) | 6 |
| IGR J17591−2342 | 90401331002 | 18-08-13 | 00010804002 (S) | 18-08-14 (S) | 0.5-10 XRT 3-78 NS | $2.85^{+0.39}_{-0.37}$ | $0.98^{+0.04}_{-0.05}$ | $49.4^{+1.5}_{-1.5}$ | $1.32^{+0.04}_{-0.04}$ | $65^{+14}_{-10}$ | 5.478 | 3.787 | 1290.83 (1269) | 7 |
| IGR J17591−2342 | 80301311002 | 18-08-17 | 0795750101 (N) | 18-09-03 (N) | 1.3-10 MOS 3-78 NS | $2.84^{+0.06}_{-0.06}$ | $0.84^{+0.02}_{-0.02}$ | $36.2^{+1.7}_{-1.7}$ | $1.79^{+0.06}_{-0.06}$ | $53.8^{+6.8}_{-5.6}$ | 2.480 | 1.714 | 2386.4 (2286) | 8 |
| IGR J00291+5934 | 90101010002 | 15-07-28 | 00031258006 (S) | 15-07-29 (S) | 0.7-10 XRT-WT 3-78 NS | $0.47^{+0.06}_{-0.05}$ | $0.58^{+0.03}_{-0.03}$ | $48.2^{+2.3}_{-2.0}$ | $1.49^{+0.05}_{-0.06}$ | $531^{+112}_{-89}$ | 7.239 | 0.780 | 1669.64 (1739) | 9 |
| IGR J1737.9−3747 | 90401312002 | 18-04-02 | 0830190301 (N) | 18-04-01 (N) | 1.3-10 PN 3-78 NS | $0.72^{+0.11}_{-0.11}$ | $0.45^{+0.02}_{-0.02}$ | $57.4^{+4.1}_{-3.9}$ | $0.97^{+0.06}_{-0.06}$ | $16.8^{+4.5}_{-3.4}$ | 0.06157 | 0.05324 | 494.27 (455) | 10 |
| IGR J17511−3057 | 90101001002 | 15-04-08 | 00031492033 (S) | 15-04-08 (S) | 1.3-10 XRT 3-78 NS | $2.34^{+0.12}_{-0.12}$ | $0.57^{+0.02}_{-0.03}$ | $41.1^{+0.2}_{-0.2}$ | 1.5 [2] | $672^{+163}_{-114}$ | 6.489 | 3.697 | 1749.8 (1593) | 11 |
| MAXI J0911−655 | 90201024002 | 16-05-24 | 00081952001 (S) | 16-05-24 (S) | 0.5-10 XRT 3-78 NS | $< 1.5$ [*] | $0.74^{+0.02}_{-0.02}$ | $48.3^{+1.0}_{-1.0}$ | $1.16^{+0.02}_{-0.02}$ | $94.3^{+11.9}_{-10.0}$ | 2.661 | 2.874 | 1212.26 (1311) | 12 |
| MAXI J0911−655 | 90201042002 | 16-11-23 | 00088013001 (S) | 16-11-23 (S) | 0.5-10 XRT 3-78 NS | $< 1.5$ [*] | $0.82^{+0.02}_{-0.02}$ | $43.9^{+1.0}_{-1.0}$ | $1.17^{+0.02}_{-0.02}$ | $102.6^{+11.6}_{-9.9}$ | 3.842 | 4.150 | 1207.09 (1215) | 12 |
| PSR J1023+0038 | 30001027006 | 13-10-19 | 00080035003 (S) | 13-10-18 (S) | 0.5-10 XRT 3-78 NS | $< 1.5$ [*] | $0.29^{+0.03}_{-0.04}$ | $44.1^{+5.8}_{-6.5}$ | $1.67^{+0.23}_{-0.17}$ | $261^{+188}_{-83}$ | 0.3091 | 0.006943 | 803.15 (765) | 13 |
| PSR J1023+0038 | 30201005002 | 16-05-07 | 00092401001 (S) | 16-05-08 (S) | 0.5-10 XRT 3-78 NS | $< 1.5$ [*] | $0.30^{+0.05}_{-0.07}$ | $51.0^{+1.5}_{-1.0}$ | 1.5 [2] | $219^{+405}_{-89}$ | 0.2938 | 0.006599 | 743.96 (744) | 14 |
| PSR J1023+0038 | 80201028002 | 17-05-23 | 0794580801 (N) | 17-05-23 (N) | 0.5-10 MOS 3-78 NS | $< 1.5$ [*] | $0.21^{+0.01}_{-0.01}$ | $62.3^{+2.7}_{-2.8}$ | $1.24^{+0.05}_{-0.04}$ | $791^{+143}_{-111}$ | 0.2907 | 0.006530 | 1175.5 (1176) | 15 |
| PSR J1023+0038 | 90301006002 | 17-06-13 | 00033012166 (S) | 17-06-13 (S) | 0.5-10 XRT 3-78 NS | $< 1.5$ [*] | $0.38^{+0.06}_{-0.06}$ | $48.1^{+1.4}_{-1.3}$ | 1.5 [2] | $107^{+97}_{-42}$ | 0.3237 | 0.007271 | 267.42 (285) | 16 |
| SAX J1748.9−2021 | 90301320002 | 17-10-11 | 00010341005 (S) | 17-10-11 (S) | 0.7-10 XRT-WT 3-78 NS | $0.99^{+0.11}_{-0.09}$ | $0.70^{+0.03}_{-0.03}$ | $53.3^{+2.2}_{-1.6}$ | $1.22^{+0.04}_{-0.05}$ | $150^{+31}_{-19}$ | 3.746 | 3.239 | 1361.56 (1433) | 17 |
| SAX J1808.4−3658 | 90102003004 | 15-05-09 | 00030034088 (S) | 15-05-09 (S) | 0.5-10 XRT 3-78 NS | $< 0.4$ [*] | $0.49^{+0.02}_{-0.03}$ | $80.5^{+10.1}_{-5.8}$ | $0.48^{+0.06}_{-0.09}$ | $197^{+84}_{-38}$ | 0.9891 | 0.1450 | 414.39 (484) | 19 |
| SAX J1808.4−3658 | 90501335002 | 19-08-10 | 00033801025 (S) | 19-08-09 (S) | 0.7-8 XRT 3-78 NS | $< 1.5$ [*] | $0.60^{+0.01}_{-0.01}$ | $58.4^{+0.8}_{-0.8}$ | $0.92^{+0.01}_{-0.01}$ | $957^{+48}_{-45}$ | 11.75 | 1.723 | 2060.97 (1901) | 20 |
| Swift J1749.4−2807 | 90701310002 | 21-03-04 | 0872392001 (N) | 21-03-04 (N) | 1.5-8 MOS 5-78 NS | $2.5^{+0.1}_{-0.1}$ | $1.13^{+0.02}_{-0.02}$ | $47.3^{+0.8}_{-0.8}$ | $0.96^{+0.01}_{-0.01}$ | $57.8^{+4.0}_{-3.6}$ | 6.137 | 3.599 | 2189.06 (1842) | 21 |

(N) XMM-Newton (S) Swift/XRT (*) Upper limit 3 $\sigma$ (1) Unabsorbed flux in the 0.5 – 100 keV energy range (2) Parameter frozen

Table VI: Spectral parameters: Model = TBABS*COMPPS+DISKBB ; redshift fixed at 0

| Source | obs ID NuSTAR | Date NuSTAR (YMD) | obs ID XMM-Newton | Date XMM-Newton (YMD) | Energy range (keV) | $N_{\rm H}$ ($10^{22}$ cm$^{-2}$) | $kT_{\rm bb}$ (keV) | $kT_{\rm e}$ (keV) | $\tau$ | $K$ (km$^2$) | $kT_{\rm in}$ (keV) | norm$_{diskbb}$ (km$^2$) | Flux$^{(1)}$ ($10^{-10}$ erg s$^{-1}$ cm$^{-2}$) | Luminosity ($10^{36}$ erg s$^{-1}$) | C-value (dof) | Figure |
|---|---|---|---|---|---|---|---|---|---|---|---|---|---|---|---|---|
| SAX J1808.4−3658 | 90102003002 | 15-04-15 | 00030034077 (S) | 15-04-15 (S) | 1.3-10 XRT 5-78 NS | $4.79^{+0.73}_{-0.79}$ | $1.27^{+0.05}_{-0.06}$ | $38.3^{+1.4}_{-1.1}$ | $1.49^{+0.04}_{-0.05}$ | $58^{+12}_{-8}$ | $0.92^{+0.03}_{-0.04}$ | $47^{+8}_{-5}$ | 23.76 | 3.483 | 2505.12 (2378) | 18 |
| IGR J16597−3704 | 90301324001 | 17-10-26 | 00010364002 (S) | 17-10-25 (S) | 1.5-10 XRT-WT 5-78 NS | $2.1^{+1.3}_{-1.1}$ | $3.35^{+0.13}_{-0.13}$ | $27.3^{+3.8}_{-3.0}$ | $1.20^{+0.15}_{-0.15}$ | $0.5^{+0.1}_{-0.1}$ | $2.05^{+0.11}_{-0.09}$ | $0.44^{+0.07}_{-0.07}$ | 6.244 | 6.188 | 1470.36 (1448) | 22 |
| IGR J17062−6143 | 30101034002 | 15-05-06 | 00037808005 (S) | 15-05-06 (S) | 0.8-10 XRT-PC 3-78 NS | $< 1.5^{(*)}$ | $0.42^{+0.02}_{-0.02}$ | $162^{+23}_{-17}$ | $0.29^{+0.04}_{-0.04}$ | $241^{+58}_{-44}$ | $1.81^{+0.06}_{-0.06}$ | $0.10^{+0.02}_{-0.01}$ | 1.573 | 1.003 | 923.4 (945) | 23 |
| IGR J17062−6143 | 30201018002 | 16-09-13 | 00081872001 (S) | 16-09-13 (S) | 1-10 XRT-PC 3-78 NS | $8.2^{+2.9}_{-3.0}$ | $1.40^{+0.04}_{-0.04}$ | $82^{+7}_{-7}$ | $0.75^{+0.05}_{-0.04}$ | $0.97^{+0.13}_{-0.11}$ | $0.65^{+0.02}_{-0.03}$ | $13.0^{+2.5}_{-1.9}$ | 0.8474 | 0.5404 | 737.48 (774) | 23 |

(N) XMM-Newton (S) Swift/XRT (*) Upper limit 3 $\sigma$ (1) Unabsorbed flux in the 0.5 – 100 keV energy range

Table VII: Spectral parameters: Model = TBABS* COMPPS+DISKBB ; redshift fixed at 0.26 (10)

| Source | obs ID NuSTAR | Date NuSTAR (YMD) | obs ID XMM-Newton | Date XMM-Newton (YMD) | Energy range (keV) | $N_{\rm H}$ ($10^{22}$ cm$^{-2}$) | $kT_{\rm bb}$ (keV) | $kT_{\rm e}$ (keV) | $\tau$ | $K$ (km$^2$) | $kT_{\rm in}$ (keV) | norm$_{diskbb}$ (km$^2$) | Flux$^{(1)}$ ($10^{-10}$ erg s$^{-1}$ cm$^{-2}$) | Luminosity ($10^{36}$ erg s$^{-1}$) | C-value (dof) | Figure |
|---|---|---|---|---|---|---|---|---|---|---|---|---|---|---|---|---|
| SAX J1808.4−3658 | 90102003002 | 15-04-15 | 00030034077 (S) | 15-04-15 (S) | 1.3-10 XRT 5-78 NS | $4.37^{+0.75}_{-0.87}$ | $1.57^{+0.06}_{-0.09}$ | $42.4^{+1.4}_{-1.1}$ | $1.40^{+0.03}_{-0.02}$ | $38.8^{+9.5}_{-5.6}$ | $0.90^{+0.03}_{-0.05}$ | $52.9^{+11.1}_{-6.3}$ | 23.67 | 3.470 | 2480.66 (2378) | 18 |
| IGR J16597−3704 | 90301324001 | 17-10-26 | 00010364002 (S) | 17-10-25 (S) | 1.5-10 XRT-WT 5-78 NS | $2.12^{+1.28}_{-1.22}$ | $4.23^{+0.19}_{-0.16}$ | $31.1^{+4.2}_{-2.8}$ | $1.13^{+0.12}_{-0.14}$ | $0.30^{+0.06}_{-0.06}$ | $2.06^{+0.12}_{-0.09}$ | $0.44^{+0.07}_{-0.07}$ | 6.238 | 6.182 | 1470.48 (1448) | 22 |
| IGR J17062−6143 | 30101034002 | 15-05-06 | 00037808005 (S) | 15-05-06 (S) | 0.8-10 XRT-PC 3-78 NS | $4.3^{+3.2}_{-2.8}$ | $1.77^{+0.06}_{-0.06}$ | $77.4^{+4.9}_{-4.5}$ | $0.79^{+0.04}_{-0.04}$ | $1.14^{+0.15}_{-0.13}$ | $0.70^{+0.03}_{-0.03}$ | $16.9^{+2.8}_{-2.4}$ | 1.604 | 1.023 | 916.01 (945) | 23 |
| IGR J17062−6143 | 30201018002 | 16-09-13 | 00081872001 (S) | 16-09-13 (S) | 1-10 XRT-PC 3-78 NS | $8.2^{+2.9}_{-3.0}$ | $1.76^{+0.05}_{-0.05}$ | $84.4^{+7.4}_{-6.7}$ | $0.74^{+0.04}_{-0.04}$ | $0.60^{+0.08}_{-0.07}$ | $0.65^{+0.02}_{-0.03}$ | $12.9^{+2.5}_{-1.9}$ | 0.8448 | 0.5388 | 737.38 (774) | 23 |

(N) XMM-Newton (S) Swift/XRT (*) Upper limit 3 $\sigma$ (1) Unabsorbed flux in the 0.5 – 100 keV energy range

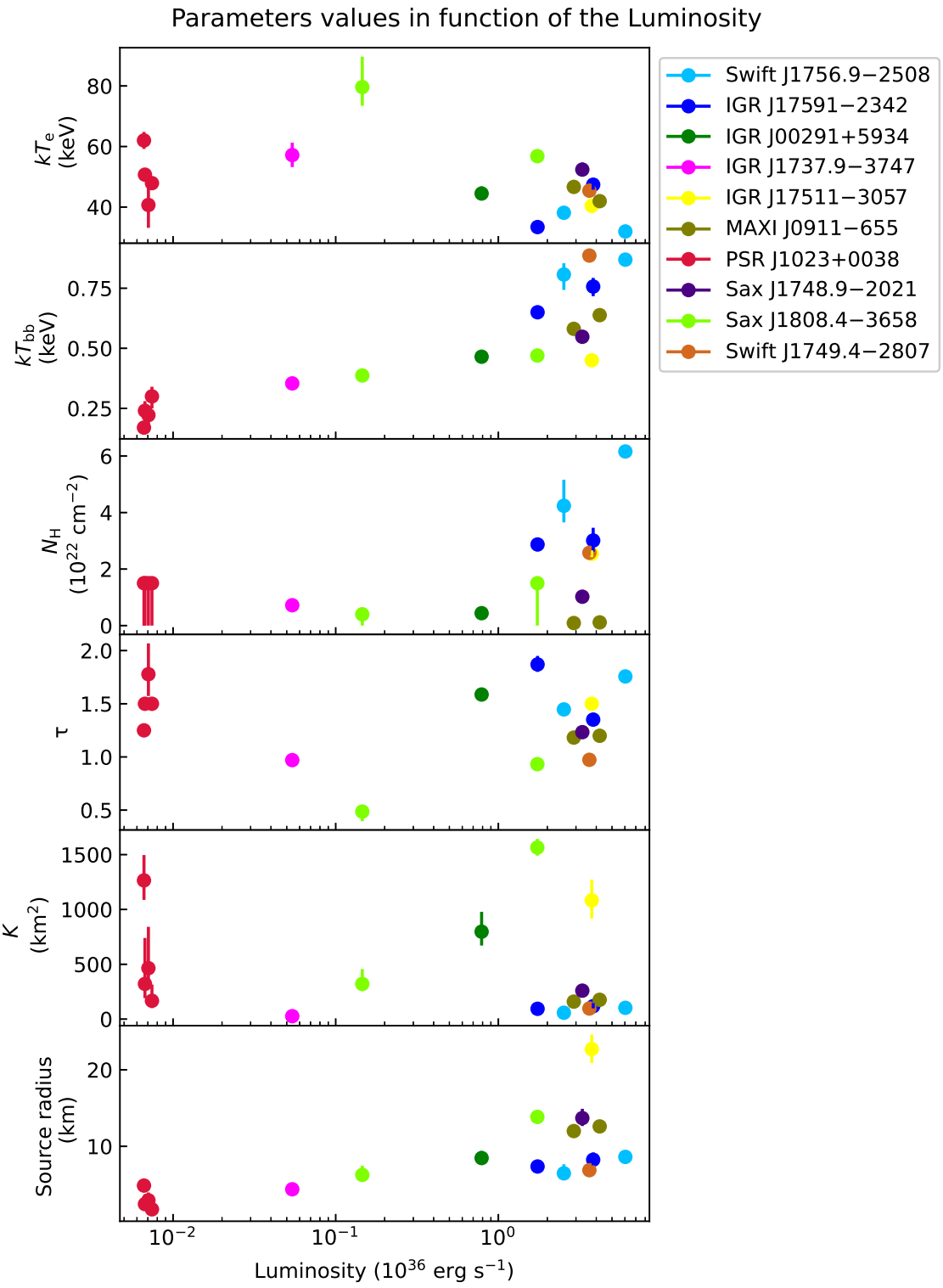


Figure 24: Parameters value in function of the Luminosity (COMPPS model, $z = 0$).

### 4.2.2 Influence of redshift on parameters

In literature, the gravitational redshift is very often fixed at 0 for the AMXPs' models. However, NSs have extremely strong gravitational field and then the associated redshift is not negligible. To be able to compare the parameters between the both redshifts used ($z = 0$ and $z = 0.26$), I divided the parameters for $z = 0$ by the same ones for $z = 0.26$. The results are shown on figure 25. Each colour corresponds to one source.

On the whole, the electron temperature ($kT_{\rm e}$) is not significantly affected by the redshift variation even if its variation is not very well constrained for PSR J1023+0038 (red point) and SAX J1808.4−3658 (green point). The gravitational redshift shifts the seed photons temperature. So, the temperature of them estimated by the model ($kT_{\rm bb}$) increased with the redshift. In average, the temperature increased by 30 % when the redshift increased from 0 to 0.26.

The hydrogen column density is not well constrained in some sources and there was no improvements by changing the redshift. The grey points on the right correspond to the two MAXI J0911−655 observations. All the $N_{\rm H}$ values are not constrained for this source, nevertheless, the 3 $\sigma$ upper limit varies with the redshift.

The normalisation parameter ($K$) is getting smaller with a greater redshift. This parameter is linked to the source radius and its distance. As the distance did not change, the source radius estimated by the model decreased with the redshift. It is consistent with the work of Xian-Feng Zhao and Huan-Yu Jia [44]. The variation of $K$ is nevertheless not similar from a source to another one and it is poorly constrained.

It is acceptable to fix a redshift at 0 instead of 0.26. Despite the seed photon

temperature is underestimated and the normalisation parameter is overestimated, the redshift variation does not change significantly the luminosity estimation of the sources or the quality of approximation.

I also tried to define the redshift as a free parameter for two sources where the fit worked well. It appears it was not possible to constrain well the redshift. In fact, the model estimated $z = 0.28^{+0.29}_{-0.22}$ or it found $z < 0.58$ (3 $\sigma$ upper limit) depending of the source. The other parameters did not change significantly but they were less constrained compared to the model with a fixed redshift. In conclusion, it seems better to freeze this parameter.

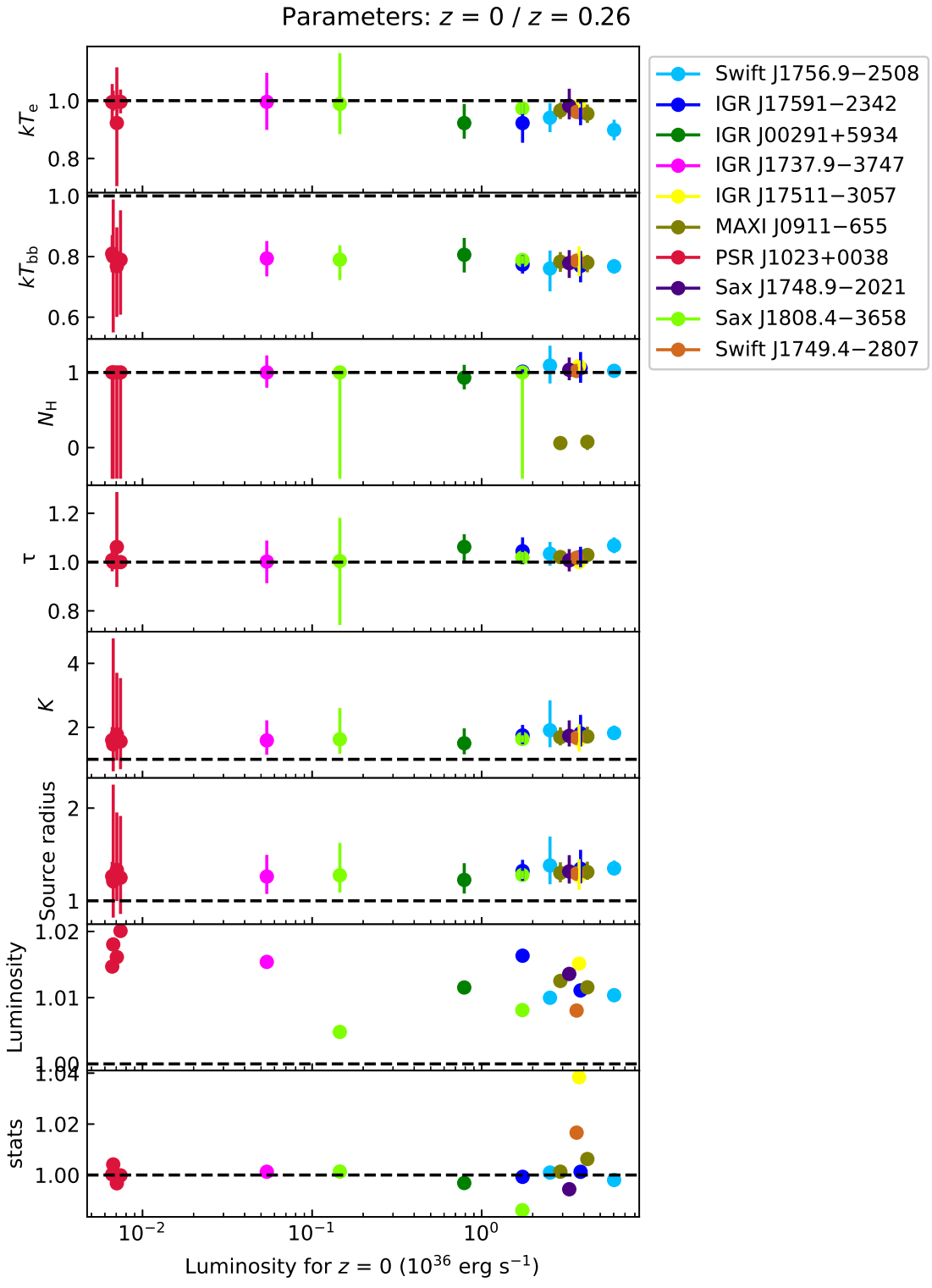


Figure 25: Ratio of parameters value for both redshifts $z = 0$ and $z = 0.26$ (COMPPS model).

# 5 Summary

I reduced the AMXPs observations performed by the NuSTAR observatory, widened the energy range with observations done by Swift/XRT or XMM-Newton to model them with the COMPPS model. It allowed to obtain a good fit for different AMXPs observations with only few exceptions. For the sources where the model did not work correctly, it was possible to have a better result simply by adding a DISKBB component to the COMPPS one without the necessity to complicate the final model with more components. It was possible to show some correlation between the seed photon temperature and the luminosity: $kT_{\rm bb}$ increases with the luminosity of the source.

Moreover, as the COMPPS model allows to fix a gravitational redshift as a parameter, I compared the values obtained when it was fixed at 0 and when it was fixed at a more physical value (0.26). It did not improve the results of spectral approximation. Nevertheless, the redshift variation increased the seed photon temperature $kT_{\rm bb}$ by approximately 30%. Also, the normalisation parameter decreased because the estimated source radius decreased with the redshift.

# References


[1] Wijnands R., van der Klis M., 1998, Natur, 394, 344.

[2] Tauris T. M., Konar S., 2001, A&A, 376, 543.

[3] Tauris T. M., van den Heuvel E. P. J., 2006, csxs.book, 623.

[4] Verbunt F., 1988, AdSpR, 8, 529.

[5] Poutanen J., Svensson R., 1996, ApJ, 470, 249.

[6] Baglio M. C., Vincentelli F., Campana S., Coti Zelati F., D'Avanzo P., Burderi L., Casella P., et al., 2019, A&A, 631, A104.

[7] de Martino D., Papitto A., Burgay M., Possenti A., Coti Zelati F., Rea N., Torres D. F., et al., 2020, MNRAS, 492, 5607.

[8] Krimm H. A., Markwardt C. B., Deloye C. J., Romano P., Chakrabarty D., Campana S., Cummings J. R., et al., 2007, ApJL, 668, L147.

[9] Sanna A., Pintore F., Riggio A., Mazzola S. M., Bozzo E., Di Salvo T., Ferrigno C., et al., 2018, MNRAS, 481, 1658.

[10] Sanna A., Ferrigno C., Ray P. S., Ducci L., Jaisawal G. K., Enoto T., Bozzo E., et al., 2018, A&A, 617, L8.

[11] Torres M. A. P., Jonker P. G., Steeghs D., Roelofs G. H. A., Bloom J. S., Casares J., Falco E. E., et al., 2008, ApJ, 672, 1079.

[12] Strohmayer T. E., Ray P. S., Gendreau K. C., Bult P. M., Guillot S., Mahmoodifar S., Jaisawal G. K., et al., 2018, ATel, 11507.

[13] Bult P., Markwardt C. B., Altamirano D., Arzoumanian Z., Chakrabarty D., Gendreau K. C., Guillot S., et al., 2019, ApJ, 877, 70.

[14] Papitto A., Bozzo E., Sanchez-Fernandez C., Romano P., Torres D. F., Ferrigno C., Kajava J. J. E., et al., 2016, A&A, 596, A71.

[15] Sanna A., Papitto A., Burderi L., Bozzo E., Riggio A., Di Salvo T., Ferrigno C., et al., 2017, A&A, 598, A34.

[16] Bond H. E., White R. L., Becker R. H., O'Brien M. S., 2002, PASP, 114, 1359.

[17] Archibald A. M., Stairs I. H., Ransom S. M., Kaspi V. M., Kondratiev V. I., Lorimer D. R., McLaughlin M. A., et al., 2009, Sci, 324, 1411.

[18] Sanna A., Burderi L., Riggio A., Pintore F., Di Salvo T., Gambino A. F., Iaria R., et al., 2016, MNRAS, 459, 1340.

[19] Bildsten L., Chakrabarty D., 2001, ApJ, 557, 292.

[20] Altamirano D., Wijnands R., van der Klis M., Patruno A., Watts A., Armas Padilla M., Cavecchi Y., et al., 2010, ATel, 2565.

[21] Ferrigno C., Bozzo E., Falanga M., Stella L., Campana S., Belloni T., Israel G. L., et al., 2010, int..work, 148.

[22] Sanna A., Bahramian A., Bozzo E., Heinke C., Altamirano D., Wijnands R., Degenaar N., et al., 2018, A&A, 610, L2.

[23] Strohmayer T. E., Arzoumanian Z., Bogdanov S., Bult P. M., Chakrabarty D., Enoto T., Gendreau K. C., et al., 2018, ApJL, 858, L13.

[24] van den Eijnden J., Degenaar N., Pinto C., Patruno A., Wette K., Messenger C., Hernández Santisteban J. V., et al., 2018, MNRAS, 475, 2027.

[25] Kuiper L., Tsygankov S. S., Falanga M., Mereminskiy I. A., Galloway D. K., Poutanen J., Li Z., 2020, A&A, 641, A37. Deller A. T., Archibald A. M., Brisken W. F., Chatterjee S., Janssen G. H., Kaspi V. M., Lorimer D., et al., 2012, ApJL, 756, L25.

[26] Burderi L., Di Salvo T., Lavagetto G., Menna M. T., Papitto A., Riggio A., Iaria R., et al., 2007, ApJ, 657, 961.

[27] Altamirano D., Watts A., Linares M., Markwardt C. B., Strohmayer T., Patruno A., 2010, MNRAS, 409, 1136.

[28] Watkins L. L., van der Marel R. P., Bellini A., Anderson J., 2015, ApJ, 812, 149.

[29] Deller A. T., Archibald A. M., Brisken W. F., Chatterjee S., Janssen G. H., Kaspi V. M., Lorimer D., et al., 2012, ApJL, 756, L25.

[30] Galloway D. K., Muno M. P., Hartman J. M., Psaltis D., Chakrabarty D., 2008, ApJS, 179, 360.

[31] Bult P., Chakrabarty D., Arzoumanian Z., Gendreau K. C., Guillot S., Malacaria C., Ray P. S., et al., 2020, ApJ, 898, 38.

[32] Galloway D. K., Cumming A., 2006, ApJ, 652, 559.

[33] Altamirano D., Cavecchi Y., Patruno A., Watts A., Linares M., Degenaar N., Kalamkar M., et al., 2011, ApJL, 727, L18.

[34] Valenti E., Ferraro F. R., Origlia L., 2007, AJ, 133, 1287.

[35] Keek L., Iwakiri W., Serino M., Ballantyne D. R., in't Zand J. J. M., Strohmayer T. E., 2017, ApJ, 836, 111.

[36] Li Z. S., Kuiper L., Falanga M., Poutanen J., Tsygankov S. S., Galloway D. K., Bozzo E., et al., 2021, A&A, 649, A76.

[37] Sanna A., Pintore F., Bozzo E., Ferrigno C., Papitto A., Riggio A., Di Salvo T., et al., 2017, MNRAS, 466, 2910.

[38] Sanna A., Bozzo E., Papitto A., Riggio A., Ferrigno C., Di Salvo T., Iaria R., et al., 2018, A&A, 616, L17.

[39] Pintore F., Sanna A., Di Salvo T., Del Santo M., Riggio A., D'Aì A., Burderi L., et al., 2016, MNRAS, 457, 2988.

[40] Di Salvo T., Sanna A., Burderi L., Papitto A., Iaria R., Gambino A. F., Riggio A., 2019, MNRAS, 483, 767.

[41] van den Eijnden J., Degenaar N., Pinto C., Patruno A., Wette K., Messenger C., Hernández Santisteban J. V., et al., 2018, MNRAS, 475, 2027.

[42] Shang L.-H., Zhang C.-M., Li D., Wang D.-H., Wang S.-Q., Wang P., Pan Y.-Y., et al., 2017, ApJ, 849, 87.

[43] Van Den Eijnden J., Degenaar N., Russell T., Wijnands R., Hernandez Santisteban J. V., Russell D. M., AlMannaei A., et al., 2018, ATel, 11520.

[44] Zhao X.-F., Jia H.-Y., 2014, RMxAA, 50, 103.